AGU ADVANCING EARTH AND SPACE SCIENCES

AGU Advances

RESEARCH ARTICLE
10.1029/2024AV001265

Peer Review The peer review history for this article is available as a PDF in the Supporting Information.

Key Points:

- 2.5-D synthetic waveform predictions and advances in array analyses allow us to localize PKP scatterer locations
- Individual scatterers are located beneath North America and beneath the western Pacific Ocean which may be generated by ultra-low velocity zones
- Mid-ocean ridge basalt melting could explain ULVZ occurrence in both locations

Supporting Information:

Supporting Information may be found in the online version of this article.

Correspondence to:
M. S. Thorne,
michael.thorne@utah.edu

Citation:
Thorne, M. S., Pachhai, S., Li, M., Ward, J., & Rost, S. (2024). Investigating ultra-low velocity zones as sources of PKP scattering beneath North America and the western Pacific Ocean: Potential links to subducted oceanic crust. *AGU Advances*, *5*, e2024AV001265. https://doi.org/10.1029/2024AV001265

Received 3 APR 2024
Accepted 25 JUL 2024

Investigating Ultra-Low Velocity Zones as Sources of PKP Scattering Beneath North America and the Western Pacific Ocean: Potential Links to Subducted Oceanic Crust

Michael S. Thorne[1], Surya Pachhai[1], Mingming Li[2], Jamie Ward[3], and Sebastian Rost[3]

[1]Department of Geology and Geophysics, University of Utah, Salt Lake City, UT, USA, [2]School of Earth and Space Exploration, Arizona State University, Tempe, AZ, USA, [3]School of Earth and Environment, University of Leeds, Leeds, UK

Abstract Seismic energy arriving before the compressional (P) wave passing through the core (PKP), called PKP precursors, have been detected for decades, but the origin of those arrivals is ambiguous. The largest amplitude arrivals are linked to scattering at small-scale lowermost mantle structure, but because these arrivals traverse both source and receiver sides of the mantle, it is unknown which side of the path the energy is scattered from. To address this ambiguity, we apply a new seismic array method to analyze PKP waveforms from 58 earthquakes recorded in North America that allows localization of the origin of the PKP precursors at the core-mantle boundary (CMB). We compare these measurements with high frequency 2.5-D synthetic predictions showing that the PKP precursors are most likely associated with ultra-low velocity zone structures beneath the western Pacific and North America. The most feasible scenario to generate ULVZs in both locations is through melting of mid-ocean ridge basalt in subducted oceanic crust.

Plain Language Summary When seismic wave energy created by earthquakes encounters features with abrupt changes in material properties some of that energy can be scattered and ultimately be recorded on seismometers. Some of the scattered energy comes from the lowermost mantle near the core-mantle boundary (CMB), but locating where on the CMB the scattered energy comes from has been challenging. Using new state of the art measurement procedures and by analyzing supercomputer simulations of seismic wave scattering we are able to improve our ability to locate scatterers. Using seismic wave energy from earthquakes occurring in the New Guinea region and recorded on seismometers in North America we have identified regions of scattering at the CMB beneath both the western Pacific Ocean and western North America. The amplitude of the recorded scattered energy is sensitive to material contrasts and is most consistent with an origin from features known as ultra-low velocity zones (ULVZs). These are thin regions sitting on top of the CMB in which seismic waves passing through them move at a much slower speed. A way to explain their existence in both settings is through partial melting of Mid-Ocean Ridge Basalt that is in the oceanic crust of subducting slabs.

1. Introduction

The characteristics of seismic anomalies at Earth's core-mantle boundary (CMB) provides distinct and critical information necessary to understand the Earth's deep mantle dynamics and its long-term thermal and chemical evolution. Precursor arrivals of the seismic phases PKIKP (a compressional wave that traverses all the way through the inner-core), named PKP precursors, have been investigated for over 60 years to probe the structures of seismic anomalies in the deepest mantle (Bolt, 1962; Gutenberg, 1958). Ever since their first discovery, the origin of these precursor arrivals has been debated. The earliest studies argued that they arose from transition layers within the outer core. However, multiple studies using seismic array analyses in the 1970s provided evidence that the PKP precursors were generated by scattering near the CMB (e.g., Haddon & Cleary, 1974; King et al., 1974; Wright, 1975). A scattering lower-mantle origin to some of the precursor arrivals is now well agreed upon, yet it is unclear what features generate them and how far up into the mantle these scattering features extend.

Over the last couple of decades weak volumetric scattering throughout the whole mantle has been argued to give rise to the majority of the PKP precursor wavefield. This inference is based on fitting envelopes of global stacks of seismograms. The earliest models assumed random media with roughly 4–8 km correlation lengths and root mean square (RMS) velocity perturbations of around 0.5%–1% (Hedlin et al., 1997; Shearer, 2007; Shearer & Earle, 2004). Yet velocity perturbations of 0.1% have been proposed as being more accurate (e.g., Mancinelli &

Shearer, 2013; Margerin & Nolet, 2003a) with previously reported higher values of RMS velocity perturbations potentially related to modeling errors (Mancinelli & Shearer, 2013). To fit the global stacks, these studies utilized 1-D modeling techniques, which included scattering in distinct 1-D layers. With this approach the timing of scattered arrivals is dependent on the depth of scatterers. Whole mantle scattering models provide a good fit to the globally averaged data. However, some localized regions of the Earth generate larger amplitude precursors that require larger, for example, 10%–15%, P-wave velocity (δV_P) perturbations (Vidale & Hedlin, 1998). Few features in the lower mantle are deduced to have such large velocity perturbations and are primarily inferred to exist within the Earth's D″ layer.

Several features have been proposed to, or could, give rise to the large amplitude PKP precursors. For example, Ultra-Low Velocity Zones (ULVZs), which are thin regions sitting on top of the CMB that can have exceptionally large P- and S-wave velocity reductions of up to 25% and 45%, respectively (Thorne & Garnero, 2004; Yu & Garnero, 2018), are thus a leading candidate for the origin of these large amplitude scatterers (e.g., Ma et al., 2019; Vidale & Hedlin, 1998; Wen, 2000; Yao & Wen, 2014). Although several factors affect PKP precursor amplitudes, the magnitude of the velocity perturbation is of primary importance. For instance, a +15% P-wave velocity perturbation could generate a similar amplitude precursor as a −15% perturbation. Ultra-High Velocity Zones (UHVZs) have been proposed (Garnero et al., 2020; Yu, 2020) with S-wave perturbations of about +7–15%. These UHVZs have been identified with S-wave sensitive seismic phases, but a mechanism for generating them has been proposed through the generation of diamond at the CMB that also strongly affects P-wave velocities. This mechanism could potentially create 15% increases in δV_P (Ko et al., 2022) and also give rise to the PKP precursors. Another potential candidate is due to topography on the CMB. A ∼40% decrease in P-wave velocity occurs across the CMB and scattering induced by sharp topographic changes could also account for the precursors (Bataille et al., 1990; Hedlin et al., 1997; Mancinelli et al., 2016). Scattering could occur from lenses of post-perovskite within the D″ region (Lay et al., 2006; van der Hilst et al., 2007), but with a P-wave velocity contrast of only a couple of percent (e.g., Murakami et al., 2007) it is unlikely that this gives rise to large amplitude PKP precursors. Scattering from subducted slab material (e.g., Frost et al., 2017; Haugland et al., 2018; Ma et al., 2016) has also been advocated to explain localized precursors. But in the lowermost mantle P-wave velocity perturbations of MORB are predicted to only be on the order of 1%–2% or less (Wang et al., 2020), thus the generation of large magnitude δV_P anomalies in a subduction setting is likely related to ULVZ or UHVZ phenomena. Ultra-High Velocity Zone generation could occur if the slab is hydrated and reacts with iron at the CMB (Ko et al., 2022). Partially molten ULVZs could be generated in the vicinity of subducted slabs through the melting of subducted MORB because of its low melting temperature (Andrault et al., 2014, 2017; Pradhan et al., 2015), giving rise to the scatterers (Festin et al., 2024; Li, 2023; Thorne et al., 2019).

In this paper we analyze seismic recordings from earthquakes that occurred in the New Guinea region and recorded in North America. This geometry samples the lower mantle on the source-side of the path beneath the western Pacific Ocean and beneath North America on the receiver-side. Because many earthquakes are generated in Indonesia at ideal epicentral distances to receivers in North America, several previous studies have identified PKP precursors originating along these paths (Bataille & Flatté, 1988; Garnero et al., 2007; Hedlin & Shearer, 2000; Ma & Thomas, 2020; Margerin & Nolet, 2003b; Waszek et al., 2015; Yao & Wen, 2014). However, attempts to differentiate scatterer locations between source- and receiver-side have been inconclusive. Yet, large enough differences in arrival angle and travel-time moveout between source- and receiver-side scatterers exist such that with modern array processing approaches it is possible to distinguish where the scatterer originates. We show that the observations are dominated by a source-side scattering region beneath the western Pacific Ocean. This scattering region is coexistent with large-scale ULVZs identified in previous studies (He et al., 2006; Idehara, 2011; Pachhai et al., 2015; Thorne et al., 2020, 2021; Yao & Wen, 2014). However, additional scattering locations beneath the western United States and Canada are also evident in these data that may also be related to ULVZ locations. Among the various hypotheses for ULVZ genesis, an origin through the subduction and subsequent melting of MORB feasibly explains ULVZ occurrence in both locations.

2. PKP Precursors

2.1. PKP Precursor Ray Paths

Ray paths of scattered arrivals from the CMB are shown in Figures 1a and 1b for source- and receiver-side scatterer locations, respectively. As we can see in this figure, the geometric ray paths of the scattered energy are

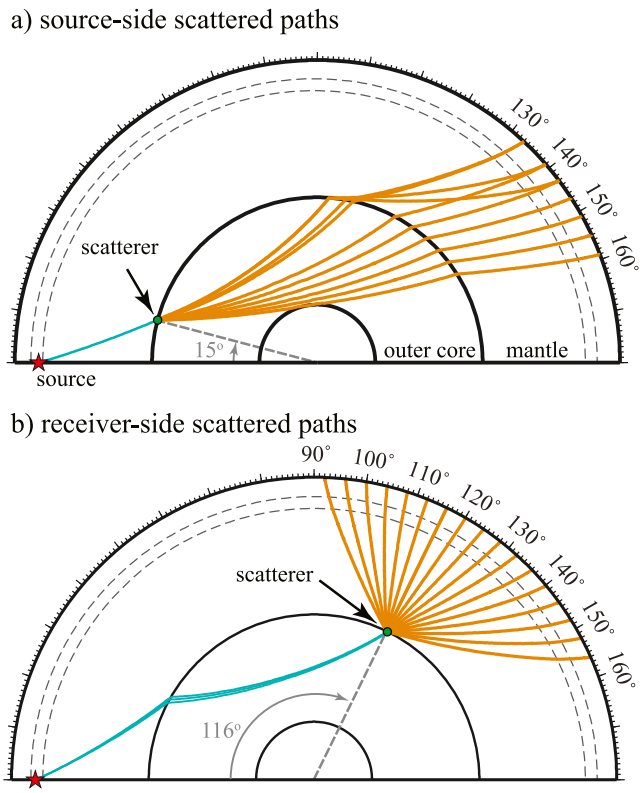

Figure 1. Ray paths for scattered PKP arrivals where the scatterer (green dot) is located either on (a) the source- or (b) receiver-side of the path. (a) The scatterer is located 15° in angular distance from the source. Here a single ray from the source to the core-mantle boundary (CMB) (blue line) reaches the scattering location. Possible scattered paths are drawn in orange that reach the receivers in 4° increments. Note that from a scatterer located on the CMB, scattered KP arrivals can occur in distances from 118° to 144° from the scatterer. So, for a scatterer located 15° from the source, the first possible scattered arrivals can occur at approximately 15° + 118° = 133°.
(b) Scatterer is located 116° from the source on the receiver side of the path. Note that multiple PK arrivals (blue lines) reach this scatterer. From this location scattered arrivals (orange lines) can geometrically reach a wider distance range than is shown in panel (a).

fundamentally different depending on scatterer location. As a result, the energy arrives at the receivers at different vertical angles (i.e., slowness) depending on whether the scatterer is located on the source- or receiver-side of the path. A scatterer located on the source-side of the path is shown in Figure 1a. Here a direct P-wave travels from the source to the CMB. From the scatterer location on the CMB the energy going through the core and back out through the mantle (the *KP* leg of *PKP*) must follow specific ray paths. In the PREM model (Dziewonski & Anderson, 1981) we can only geometrically ray trace KP arrivals in distance of 118°–144° from this specific scatterer location. This means if we have a scatterer located at an angular distance of 15° from the source then we will first observe a scattered arrival at 15° + 118° = 133°. On the other hand, if a scatterer is located on the receiver-side of the path (Figure 1b) we should be able to observe scattered arrivals at any epicentral distance if their amplitude is large enough to detect and the arrival time is still ahead of PKIKP. In Figure 1 we only show ray paths for arrivals that have been scattered once, noting that multiply scattered arrivals are also possible (e.g., Margerin & Nolet, 2003b).

2.2. 2.5-D Synthetic Waveform Predictions

The inferences drawn from the ray path diagrams shown in Figure 1 are verified by full waveform modeling. Previous efforts at modeling the scattering of PKP precursors have primarily used 1-D methods and have shown minimum travel-time curves for scattered waves from certain depths within the Earth (e.g., Hedlin & Shearer, 2000; Mancinelli et al., 2016). Ray theoretical calculations show that a minimum travel-time exists for scatterers occurring at the CMB and that scattering at times closer to PKIKP may occur from shallower depths. However, it is important to note that the minimum CMB scattering time only occurs for arrivals scattered at certain angular distances from the source. Here we use the PSVaxi finite difference algorithm to compute full wavefield synthetic seismograms (Jahnke, 2009). The PSVaxi technique computes the seismic wavefield on a 2-D grid which is virtually rotated about an axis of symmetry passing through the earthquake source and the center of the Earth. This method provides correct 3-D geometric spreading for a 2-D input model. The PSVaxi technique has been used in several previous deep Earth studies (e.g., Jensen et al., 2013; Krier et al., 2021; Thorne et al., 2013; Vanacore et al., 2016). Here, we compute synthetic seismograms with dominant periods of 2 s to show the primary features observed in the PKP-precursor wavefield. This allows us to explore both variations in depth (as in the 1-D techniques) and lateral variations.

We compute synthetics for ULVZ and UHVZ heterogeneities for box-car shaped anomalies. Figure 2 shows our model geometries. For these models, we define the length of the ULVZ or UHVZ heterogeneity in the great circle arc distance as l, the thickness of the heterogeneity as h, and the angular distance to the leading edge of the heterogeneity as l_1. The elastic parameters of S-wave velocity (δV_S), P-wave velocity (δV_P), and density ($\delta\rho$) are perturbed within the heterogeneity. Models of CMB topography are computed as random media generated with a RMS topographic variation of 2 km with a 20 km correlation length with a von Karman autocorrelation function (Frankel & Clayton, 1986). Plots of the topography models shown are given in the online supplements (Figure S12 in Supporting Information S1).

2.3. PKP Precursors Generated by Lateral Heterogeneities

As discussed above, ULVZs are a good potential source of large amplitude PKP precursor arrivals and represent features located in finite regions of the CMB. Here we use these features to demonstrate the effect of lateral variation in scatterer position on the CMB on the PKP precursor wavefield noting that these observations can be extended to other finite heterogeneities such as CMB topographic anomalies. Synthetic predictions for a ULVZ

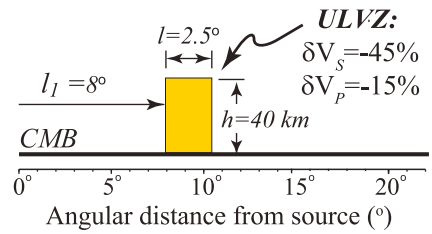

Figure 2. A schematic of the boxcar shaped ultra-low velocity zone (ULVZ) model definitions used in this paper for a position of $l_1 = 8°$ and a length (l) of 2.5°. The l_2-edge is located $l_1 + l = 10.5°$. Note that in this figure the ULVZ is vertically exaggerated to focus on the nomenclature we use in defining ULVZs. A 2.5° length ULVZ would be 152 km along the core-mantle boundary, or roughly 4× the ULVZ height.

located on the source-side of the path are shown in Figures 3a and 3b. The ULVZ model is a simple box-car shaped model with S-wave velocity reduction (δV_S) of −45% and P-wave velocity reduction (δV_P) of −15% which is at the larger end of potential ULVZ elastic parameters (Yu & Garnero, 2018). The ULVZ has a thickness (h) of 40 km and is 2.5° in length in the great circle arc direction. Figure 3 shows different ULVZ positions based on their angular distance from a line passing through the earthquake source and the center of the Earth (l_1). The positions of the near source edge are $l_1 = 10°$ (Figure 3a) and $l_1 = 15°$ (Figure 3b). For these box-car shaped ULVZs scattered arrivals originate at both edges (l_1 and l_2 as the edge into the receiver direction) of the ULVZ. Hence for the model predictions shown in Figure 3a, a scattered arrival is generated at the ULVZ l_1-edge (10°) and at the l_2 edge (10° + 2.5° = 12.5°). For a source-side scatterer located on the CMB, scattered KP arrivals can occur in distances from 118° to 144° from the scatterer as ray traced through the PREM model. Thus, in Figure 3a, we should observe two scattered arrivals that are first observable at epicentral distances of 10° + 118° = 128° (for the l_1 edge) and 12.5° + 118° = 130.5° (for the l_2 edge). Both arrivals are evident in Figure 3a. The scattered arrival from the l_2 edge arrives first and is marked with the magenta circle labeled *A* in Figure 3a. We first observe this arrival around 131° in the synthetic predictions which agrees with the ray theoretical predictions. The scattered arrival from the l_1 edge arrives second (marked with the magenta circle labeled B in Figure 3a) which we first observe around 127° (see also Figures S13–S15 in Supporting Information S1 for the sensitivity of PKP amplitudes and travel-times with respect to ULVZ parameters). Slight differences may exist in these synthetic predictions because they are computed with a modified version of PREM in which the crust and upper mantle discontinuities are smoothed over to reduce the complexity of the wavefield in the elastic synthetic seismograms. For a scatterer located at 15° we see that the precursors arrive earlier in time but are only visible at longer epicentral distances. These synthetics demonstrate several important points about scatterers located on the source-side: (a) Even though these scatterers are located on the CMB, arrival times do not necessarily coincide with the ray-theoretical CMB minimum scattering time curve (drawn in orange in Figure 3) and may come in several seconds later. (b) Scattered arrivals are only observed across a limited range of epicentral distances that depends

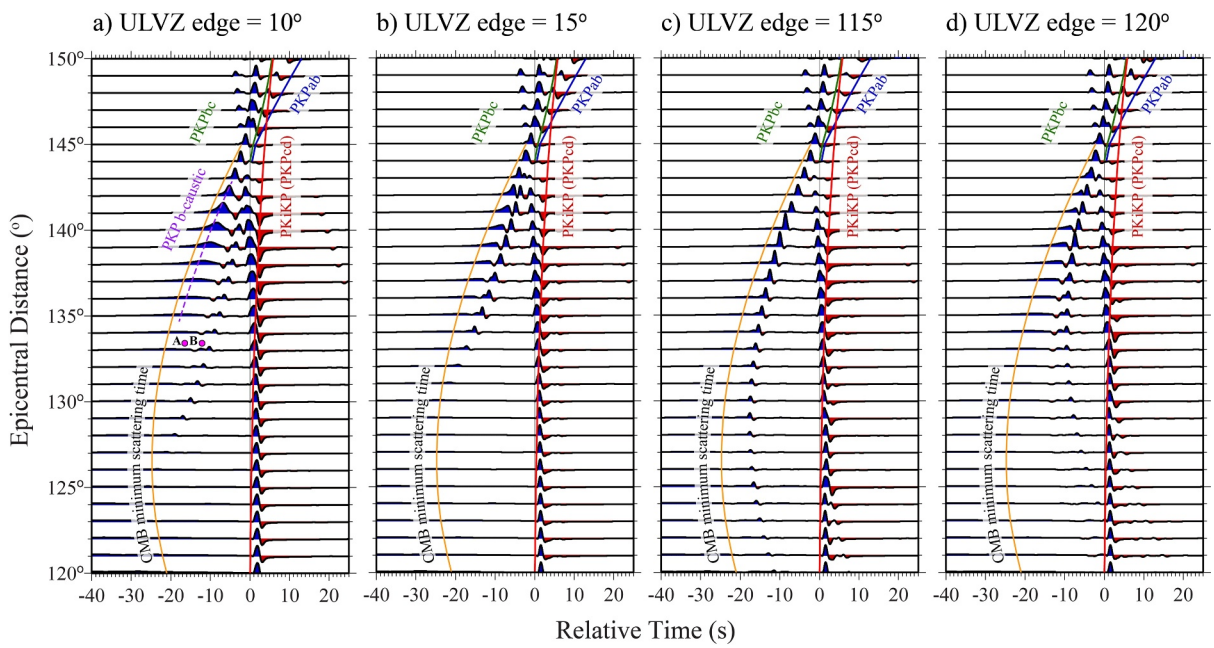

Figure 3. Synthetic seismogram predictions for a ultra-low velocity zone (ULVZ) heterogeneity. Each model has a ULVZ with $\delta V_S = -45\%$, $\delta V_P = -15\%$, density increase of 10%, thickness = 40 km, length in the great circle arc direction = 2.5°. Models vary in the position of the ULVZ edge nearest to the source such that (a) $l_1 = 10°$, (b) $l_1 = 15°$, (c) $l_1 = 115°$ and (d) $l_1 = 120°$. Two distinct scattered arrivals are marked with magenta circles and labeled A and B in panel (a). Shown are vertical component displacement seismograms aligned in time on the PREM predicted PKIKP travel time.

on scatterer location. (c) PKP precursor slowness should occur within the range of ∼2.8–4.3 s/°. (d) At the largest epicentral distances (starting around 138°) we also observe an arrival that has been described as a diffraction from the PKP b-caustic (Buchbinder, 1974; Schlittenhardt, 1996; Thomas et al., 2009). These are the long period arrivals coming in just before the precursors (indicated by the dashed purple line in Figure 3a) visible to roughly 138° near the CMB minimum time curve. Previous studies have described this arrival to have a distinctive slowness of 3.5 s/° (e.g., Schlittenhardt, 1996) which is similar to the slowness for source-side scattered arrivals, but deviates from the slowness for a diffracted P-wave at the CMB. Thus, one must also be careful not to confuse this arrival as a scattering related precursor, and to be especially cautious in searching for source-side precursor arrivals. In order not to confuse this arrival with a potential scatterer we limit the epicentral distance range in which we search for precursors to be less than 137°.

Synthetic predictions for receiver-side scatterers are shown in Figures 3c and 3d. When the ULVZ l_1-edge is located at 110° no PKP arrivals reach this position in the PREM model for a 500 km deep event, and we do not observe any precursory energy. When the l_1-edge is located at 112.5°, we observe one scattered arrival originating from the l_2- ULVZ edge located at 115°. In contrast to the source-side scatterers, here we see that the arrival agrees with the CMB minimum time curve. In Figure 3c, the l_1-edge is located at 115° and l_2-edge is located at 117.5°. Here the precursor arrival from the l_1-edge follows right along the CMB minimum time curve but of low amplitude and difficult to identify in these synthetics and likely not observable in data. The larger amplitude precursor arising from the l_2-edge comes in a few seconds later and dominates the precursor wavefield in this model. In Figure 3d the l_1-edge is at 120° and we can clearly see two precursor arrivals which are shifted in time significantly from the minimum scattering time. In addition, we see a more complex pattern of PKP postcursors at shorter distances (∼120°–127°). When a precursor arrival is generated on the receiver-side of the path it may be observed at all distances following a curve that is similar in shape to the minimum time curve. But the actual arrival time may be several seconds behind this curve. These precursor arrivals all have significantly lower slownesses than source-side PKP precursors. At an epicentral distance of 135° we predict slownesses from approximately 1.5 to 2.5 s/° indicating a steeper incidence angle at the surface, which is in agreement with the ray paths shown in Figure 1b.

3. PKP Data Set

We searched for earthquakes occurring in the New Guinea region that satisfy the following criteria: (a) latitudes of ±10° and from longitudes of 115°–135°, (b) events with depths ≥75 km and magnitudes $M_W \geq 5.8$, (c) in the epicentral distance range from 120° to 150° recorded in North America. We considered broadband seismic records from 2008 to 2022 available through the Incorporated Research Institutions for Seismology Data Management Center (IRIS DMC). The start time of our data collection coincided with the start of the Earthscope project when data density became large enough to perform array analyses. We initially found 98 events meeting these criteria. We next visually inspected record sections of these data and removed events with obvious source-time function complexity, or few waveforms in the distance range from 120° to 140° where precursors can be observed. After this initial quality control step, we retained 58 high quality events (Table S1 in Supporting Information S1). Processing steps on individual records consisted of detrending the traces, removing the instrument response, and bandpass filtering in a frequency band with corners from 0.7 to 2.3 Hz. We calculated the SNR of individual records relative to the PKIKP arrival and removed all traces with SNR ≤4. This left us with 25,688 high-quality vertical component seismic traces. The data distribution for our final data set is shown Figure S1 in Supporting Information S1.

Two example record sections are shown in Figure 4. The record sections are drawn in a restricted azimuthal window of ±5° with respect to a given azimuth. For example, in Figure 4a, the central azimuth is 40° (green line in map view of Figure 4a) and thus only records are drawn with azimuths from 35° to 45° (red triangles in Figure 4a). Narrow restricted azimuthal range allows us to see potential receiver-side precursors in the record sections that may get stacked out to nothing if we look at all azimuths at once. The examples shown in Figures 4a and 4b show what appears to be constant slowness (3.8 s/°) energy at distances shorter than 143°. This retrograde arrival becomes longer period and dies out as it approaches 137°. Then we observe a large amplitude precursor arrival that is delayed in time with respect to the diffracted arrival. This precursor arrival is apparent from ∼132° to 137° but suddenly drops to an immeasurable amplitude at ∼131°. This precursor appears similar in appearance to the synthetics for a source-side scatterer shown in Figure 3b. Similar large amplitude precursors are observed for

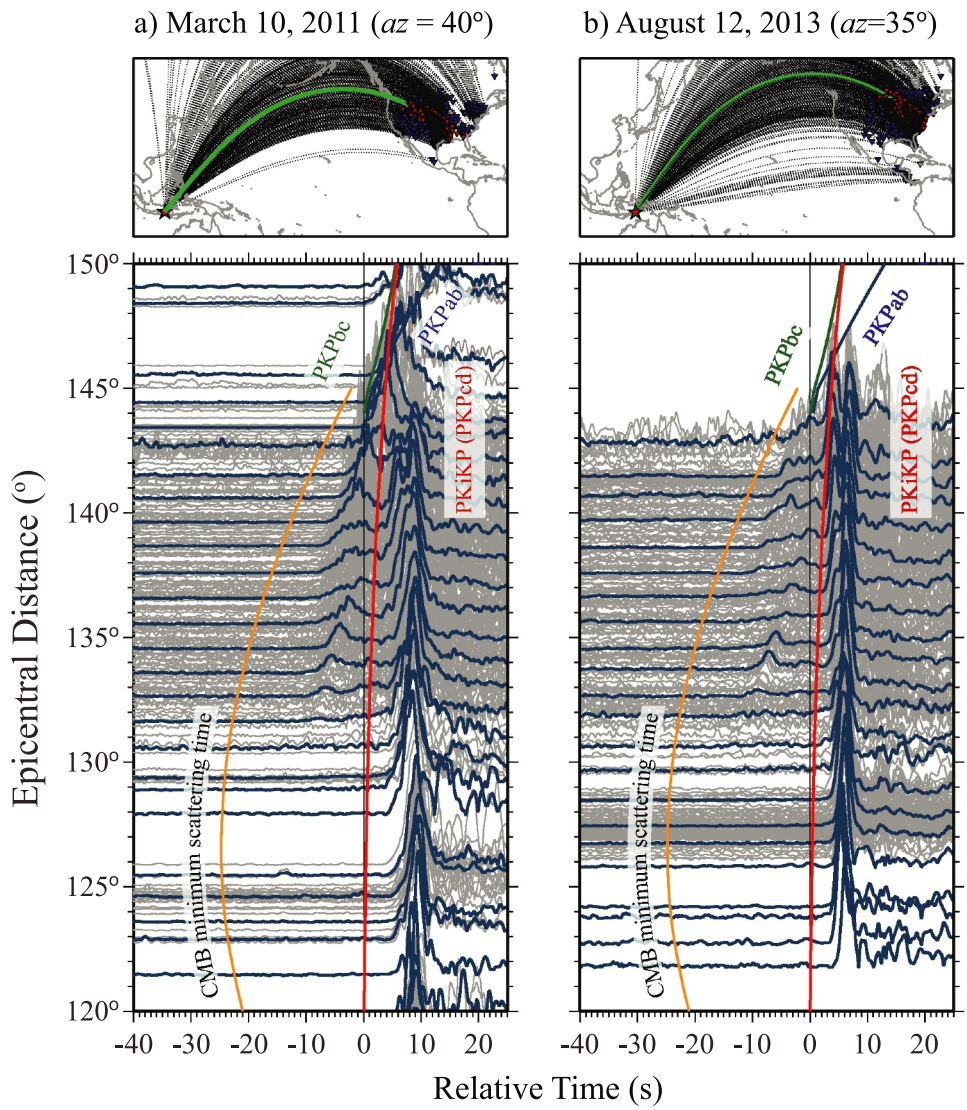

Figure 4. Example record sections for data used in this study. Data are shown for three events (a) 10 March 2011, 17:08 (event depth = 510 km, M_W = 6.5), and (b) 12 August 2013, 00:53 (event depth = 95 km, M_W = 6.0). In each panel the record sections are drawn using data within ±5° of the azimuth indicated. For example, in panel (a), only data with azimuths between 35° and 45° are shown in the record section. A reference map is given above each record section. In these maps, the reference azimuth is drawn with the heavy green line. All stations that went into making the azimuthal bin record section are drawn as red triangles, whereas all stations for that event are indicated by blue triangles. The event location is drawn with a red star. For the record sections, individual seismic traces are shown in gray and linear stacks in 1° epicentral distance bins are drawn in blue. Envelope traces are shown, bandpass filtered between 0.7 and 2.3 Hz.

many of the events occurring in this region (see Figures S2–S11 in Supporting Information S1 which shows record sections for all events used in this study).

4. Array Methods

We use the automatic array processing methods of Ward et al. (2021, 2023) to identify precursor arrival times, slowness, and back-azimuth. We project the likely scattering locations to the CMB using ray tracing through a 1-D Earth model and compare our observations with 2.5-D synthetic predictions for models with lateral seismic velocity heterogeneities. This is fundamentally different from 1-D modeling approaches in that variations in travel-time of the scattered arrivals can be accommodated by lateral variations in scatterer locations and not just in the depth of the scatterer.

4.1. Automatic Array Processing

Measuring PKP precursor slowness using seismic array data can provide a means of resolving the source-/receiver-side ambiguity since the slowness is related to the angle of the incoming energy which can be significantly different for source-versus receiver-side scatterers (Husebye et al., 1976). However, for small-scale seismic arrays, the slowness uncertainty obtained can be greater than 1 s/° which may not be good enough to resolve the difference between source- and receiver side scattering. Slowness resolution improves with increasing aperture and some previous efforts have used some of the largest of the International Monitoring System arrays such as NORSAR, Yellowknife (YKA), or Warramunga (WRA) to distinguish source-versus receiver side scattering (Cao & Romanowicz, 2007; Doornbos, 1976; King et al., 1974). Although established arrays can localize scatterer location, their fixed locations limit the deep Earth areas that can be searched. The proliferation of seismic instruments in recent years provides enough station density to allow construction of virtual seismic arrays by grouping together closely located seismometers. Several studies have successfully used large (∼5° diameter) virtual arrays to explore lower mantle heterogeneity (e.g., Ward et al., 2023; Whittaker et al., 2016). In traditional array processing techniques, the slowness measurement error is unknown. However, recent advances in seismic array processing techniques have enabled the ability to accurately measure errors in slowness, backazimuth, and travel-time promising greater reduction in the uncertainty associated with array measurements (Korenaga, 2013; Ward et al., 2021, 2023).

To take advantage of array processing techniques, we group the receivers into virtual subarrays with a 2.0° radius and keep subarrays with a minimum of 8 stations. For each virtual subarray, we measure the horizontal slowness and backazimuth of the arrivals using the automatic array analysis of Ward et al. (2021, 2023). We give a brief overview of the method here, but for details about optimal parameters see Ward et al. (2021). The technique creates N bootstrap samples (with replacement) of the seismic waveforms recorded at the subarray in question. Then for each bootstrap sample, beamforming (Rost & Thomas, 2002) corrected for a curved wavefront is applied (Ward et al., 2020). For each of the resulting power grids, the top M peaks are retained. The assumption here is coherent arrivals will have high power across the bootstrap samples. All the peaks from all bootstrap samples are gathered and then clustered using the density-based clustering algorithm DBSCAN (Ester et al., 1996). Note, if there are no dense clusters (each bootstrap sample giving very different slowness vector estimates) DBSCAN will return zero clusters and no arrival identified. From each cluster, we create a histogram of the full slowness vector components and thus measure the horizontal slowness and backazimuth by taking the mean along with their associated uncertainties via their standard deviation. In this paper, we extend this technique by also measuring the travel time of the arrivals with uncertainties. To do this, we iterate through all slowness vector properties in a given cluster. Using these slowness vectors, we shift and stack the seismograms recorded at the sub array and form a beam. There should be the same number of beams as points in the cluster. For each beam, we calculate the seismic envelope and record the time of the maximum amplitude. This then gives a distribution of arrival time estimates from which we can take a measurement (mean) and an uncertainty (standard deviation). We tested this array processing technique to observations filtered with a wide range of filter bands. We decided that a filter with corners from 0.7 to 2.3 Hz worked best to isolate the precursory arrivals and suppress the microseismic noise.

We estimated the noise in the records by shifting each time series by a randomly generated time within ±15 s of the reference phase (PKIKP). These time shifted waveforms are stacked, and power of the beam was measured. This was repeated 1,000 times and the mean value of the power was taken as noise. Any beam power less than noise was set to zero. From the resulting power distribution, we took up to 3 peaks to describe the slowness vectors of possible arrivals. We then apply DBSCAN to find the clusters of slowness vectors. This clustering approach identifies the clusters by their density by requiring a cluster to have a minimum number of points for a given radius. Here, we use 0.2 s/° for the radius and 25% of bootstrap samples for the minimum points. Note points that are not dense enough are classified as noise. Once the clusters are formed, we also estimated the uncertainty in slowness vector by calculating the standard deviation of backazimuth and horizontal slownesses in each cluster. First, we applied this technique in a window around the main PKIKP arrival to obtain a reference time for each virtual array. We then applied the technique in the precursor time window with the main PKIKP arrival windowed out. We used a 30 s wide time window from 33 to 3 s ahead of the PKIKP arrival as previously determined. Individual arrivals are then found from the cluster analysis. For each subarray and each event, we retain the seismic arrival information, particularly the relative travel-time, slowness, backazimuth, and their associated errors.

4.2. Scattering Likelihood

We search among the candidate arrivals retained from the array processing approach to determine if any of them are consistent with a CMB origin. We do this by generating a grid of locations on the CMB and for each grid point we calculate the theoretical travel-time, slowness, and backazimuth. Because we have potential scatterer locations across a wide range of latitudes, we generate a Fibonacci grid which creates a nearly uniform grid (Swinbank & Purser, 2006). On the surface of a sphere, we set up the grid with points ranging from $i = -N$ to $+N$. For this study, we let $N = 240{,}000$. This gives an average grid spacing of ~0.27° (16 km on the CMB). The latitude (λ) of the *ith* grid point is determined as:

$$\sin \lambda_i = \frac{2i}{2N+1}, \tag{1}$$

and the longitude (θ) is given by:

$$\theta_i = (i \; modulo \; \phi)\left(\frac{2\pi}{\phi}\right), \tag{2}$$

where $\phi = \frac{1+\sqrt{5}}{2}$ is the golden ratio. Based on our data coverage we defined two separate grids for potential source- and receiver-side scatterer locations. In practice, we calculated a single Fibonacci grid and only included grid points for (a) a source-side region: $-10° \le \lambda \le 30°$ and $110° \le \theta \le 160°$ and (b) a receiver-side region $+10° \le \lambda \le 70°$ and $-150° \le \theta \le -50°$.

We utilize a technique presented in Kaneshima and Helffrich (1998) to locate potential scatterers. For each geographic bin that we have a candidate precursor we calculate the likelihood of the precursor arising from a grid point in our grid as defined above. At each grid point we calculate the travel-time (t_i), horizontal slowness (u_i), and backazimuth (b_i) for a scattered arrival coming from that grid point by ray tracing with the Tau-P toolkit (Crotwell et al., 1999). We measure the observed travel-time (t_0), slowness (p_0), and back-azimuth (b_o) and their associated errors (ε_t, ε_u, and ε_b) as described above for the observation. Then for the *ith* grid point we can define the likelihood (L) that the precursor originates from that location as:

$$L_i = e^{\left[-\frac{(u_i-u_0)^2}{\varepsilon_u^2} - \frac{(b_i-b_0)^2}{\varepsilon_b^2} - \frac{(t_i-t_0)^2}{\varepsilon_t^2}\right]}. \tag{3}$$

Example travel-time, slowness, and back azimuths for a single event are shown in Figure 5. The calculations in this example are shown on our grid for a 510 km deep event occurring on 10 March 2011, for an epicentral distance of 135° (event 22 in Table S1 in Supporting Information S1). Figure 5a shows the travel-time relative to the theoretical PKIKP travel-time for the source-side grid. Here we can see that precursors can arrive within a finite area (bluish colored negative travel-times). The gray shaded grid points indicate that no scattered PKP arrival can arrive at the receiver from those points. In this example the arrival must have a slowness between 2.80 and 4.03 s/° and within ±17.5° of the great circle arc backazimuth. At this distance, the minimum travel-time for a precursor is −17 s with respect to PKIKP and can only occur if the scatterer is on the great circle path. The effects of the uncertainty measurements on the likelihood function are shown in Figures S12–S14 in Supporting Information S1.

On the receiver-side (Figure 5e), we see a shift to lower slownesses (steeper arrivals, see Figure 1b) between 1.85 and 3.65 s/°. Although arrivals on the receiver-side of the path tend toward lower slownesses, there is still some overlap in the slowness range between source- and receiver-side scatterers. Nonetheless a low slowness around 2.0 s/°, for example, would be resolved to lie on the receiver side if the error were <0.8 s/°.

5. Results

We searched for precursor arrivals using an automatic array analysis technique (Ward et al., 2021) and plot the detected arrivals as shown in Figure 6. Note that in Figure 6, we do not show the actual slowness value of an individual detection but characterize arrivals by the expected slowness for source and receiver side slowness on a

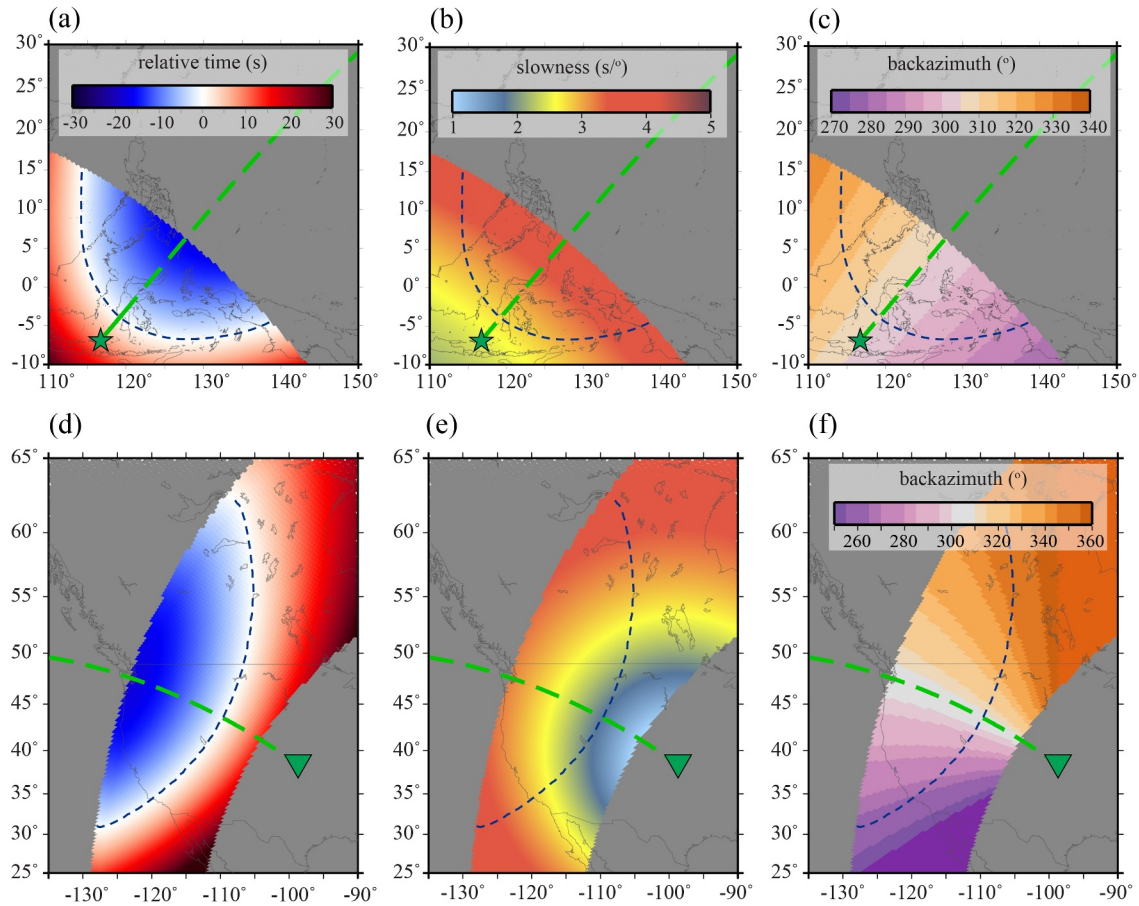

Figure 5. Example scattering parameters that can be measured for a source-side (a–c) and receiver-side (d–f) scatterer. The examples are shown for a 510 km deep event (10 March 2011) located at 6.873° and 116.72° (e) The receiver is located at 38.4225° N, 98.7112° W, and thus the backazimuth from receiver to source is 305° and the great circle arc distance is 135°. Each grid point represents the location of a hypothetical PKP scatterer. In each panels (a–c) the green star shows the event location and in panels (d–f) the green triangle shows the receiver location. The green dashed line shows the great circle arc path. (a, d) At each grid point (with locations as defined by Equations 1 and 2) we plot the travel-time for a PKP precursor originating at this location as a shaded circle. The time is shown relative to the PKIKP arrival. Thus, negative times (bluish circles) arrive ahead of PKIKP and are precursors. Positive times (reddish circles) arrive after PKIKP (post-cursors). The zero time is indicated by a dashed purple line and is repeated in all other panels. (b, e) The slowness is shown for an arrival originating from each grid point. (c, f) The backazimuth is shown for an arrival originating from each grid point. Note that we only show grid points where a PKP precursor can reach the receiver. If no PKP geometric arrival exists, then the grid point is shaded gray.

variable color scale to highlight where the scatterer originates. At each epicentral distance a scattered signal from the CMB may arrive at the receiver over a range of slownesses which depends on earthquake depth. Table 1 provides the range of slownesses for source and receiver-side scatterers for a 500 km deep event. Arrivals scattered from the receiver-side of the path typically arrive with lower slowness than arrivals scattered from the source-side of the path but with slowness overlap for specific distances. For a 500-km deep event, scattered arrivals recorded at distances <127° have no overlap in slowness. For example, a receiver-side scatterer recorded at 125° may arrive within a slowness of 0.53 s/° $\leq u \leq$ 3.05 s/°. A source-side scatterer may arrive with a slowness of 3.27 s/° $\leq u \leq$ 4.03 s/°. In Figure 6, these arrivals are plotted as blue or red, respectively. For arrivals recorded at larger distances, there is a region of overlap where the measured slowness does not uniquely constrain source- versus receiver-side scattering. We plot these arrivals as light gray. In this way, we can quickly determine if the slownesses of the PKP precursor arrivals we measure are consistent with source- or receiver-side scatterers or if the measurement is ambiguous. Actual values can be referenced to Table 1 for panel (a) where the event depth is 510 km, noting that for other depths these values are only approximate.

Before analyzing the arrivals for scattering locations, we first remove some of the arrivals that may be contaminated by source complexity or other interfering arrivals. For some events, we see arrivals at a constant time a few seconds before PKIKP. For example, in Figure 6a, we see an arrival at approximately −3 s across the

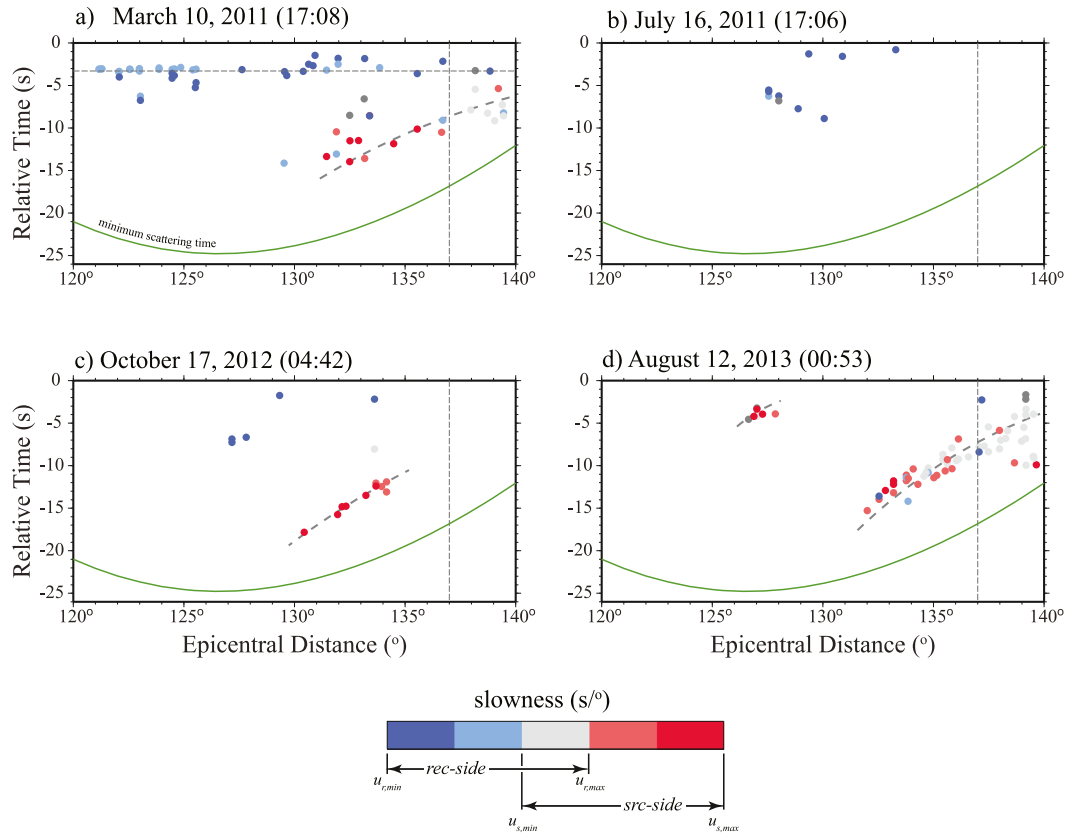

Figure 6. Measured slowness and travel-time as a function of epicentral distance for four events: (a) 10 March 2011 (event 22 in Table 1), (b) 16 July 2011 (event 23), (c) 17 October 2012 (event 28), and (d) 12 August 2013 (event 29). Individual observations are shaded by slowness on a variable scale to indicate whether the arrival is consistent with a source-side (reddish) or receiver-side (bluish) slowness. Arrivals shaded with light gray indicate overlap in slowness between source- and receiver-sides. Dark gray arrivals are out of the defined slowness bounds. In each panel, the green line indicates the core-mantle boundary minimum scattering time, and a vertical dashed line is drawn at 137° because arrivals at larger distances may be contaminated with arrivals related to another seismic phase.

entire distance range. The PKIKP arrival is slightly complicated and an additional arrival, likely part of the source-time function, consistently exists at about −3 s. Our first step is to analyze all the events and see if source-time function complexity is included in the results and remove them. For this example, we simply remove all arrivals from −3 to 0 s from further analysis. Second, the detected precursors show evidence for arrivals that are known to originate with a constant velocity of 3.8 s/° (associated with what is referred to as the PKPb-caustic) (Schlittenhardt, 1996). We did not observe this arrival for epicentral distances <137° in our synthetic models, and we do not consider arrivals with epicentral distances >137° to avoid contamination from this non-scattered arrival. The vertical dashed line in Figure 6 shows the range of arrivals that we excluded from our analysis. What is left are arrivals likely related to scattering that can be interpreted with regards to their location at the CMB.

The most common observation is a series of arrivals from 130° to 137° that show a concave downward moveout in time versus distance space (see dashed gray lines in Figure 6). These arrivals dominantly have a slowness in agreement with source-side scattering (reddish color–Figures 6a, 6c, and 6d) but may sometimes have a slowness that overlaps with the receiver-side slowness in the ambiguous range. These arrivals with the concave downward time versus distance behavior coincide with a large amplitude precursor observed in these data. More sporadically, we also observe arrivals that are consistent with a receiver-side slowness. Typically, these arrivals occur later (i.e., closer to PKIKP) than those in the source-side trend (see Figure 6c for example). But we often see these arrivals interspersed within the source-side observations (Figures 6a and 6d) and in one case (Figure 6b) only observe receiver-side scattered arrivals.

Table 1
Precursor Slowness Ranges for a 500 km Deep Source

	Source-side precursors		Receiver-side precursors	
Δ (°)	$u_{s,min}$ (s/°)[a]	$u_{s,max}$ (s/°)[a]	$u_{r,min}$ (s/°)[b]	$u_{r,max}$ (s/°)[b]
120°	3.54	4.03	0.00	2.65
121°	3.48	4.03	0.07	2.76
122°	3.43	4.03	0.18	2.83
123°	3.38	4.03	0.29	2.92
124°	3.32	4.03	0.40	2.99
125°	3.27	4.03	0.53	3.05
126°	3.23	4.03	0.64	3.13
127°	3.19	4.03	0.77	3.22
128°	3.14	4.03	0.89	3.27
129°	3.10	4.03	1.03	3.33
130°	3.06	4.03	1.18	3.40
131°	3.01	4.03	1.31	3.45
132°	2.97	4.03	1.46	3.48
133°	2.93	4.03	1.62	3.53
134°	2.90	4.03	1.77	3.58
135°	2.87	4.03	1.93	3.61
136°	2.83	4.03	2.11	3.67
137°	2.81	4.03	2.27	3.71
138°	2.78	4.03	2.46	3.75
139°	2.76	4.03	2.65	3.77
140°	2.75	4.03	2.85	3.81

[a]$u_{s,min}$ and $u_{s,max}$ are the minimum and maximum possible slownesses for a source-side PKP precursor. [b]$u_{r,min}$ and $u_{r,max}$ are the minimum and maximum possible slownesses for a receiver-side PKP precursor.

Results of the scattering likelihood analysis are shown in Figure 7. These plots show the likelihood of scattering origin for the analyzed precursors for all events and geographic bins combined. The scattering likelihood for each scattered arrival was measured. Then to combine the arrivals, they are summed and renormalized between 0 and 1. We did not calculate the likelihood product, because not every event picked up all the same scattering zones and thus using the product essentially multiplies all grid points by zero. In Figure 7 the grayed-out areas show regions in which we do not have coverage for potential PKP precursors. This is determined by calculating the relative time for each source and receiver array pair, such as is shown in Figures 5a and 5d. For each grid point on the CMB, a PKP precursor could be detected if the relative time is less than zero. For each event/array pair we determine all points on the CMB that could give rise to a precursor. All event/array pairs are combined (see Figures S15 and S16 in Supporting Information S1) to determine the total coverage.

On the source-side of the path we see that beneath the western Pacific Ocean three primary zones identifying high scattering likelihood stand out with two areas beneath the Philippine Sea area, and an additional region stretching from the Celebes Sea in the North to the Molucca Sea in the south (Figure 7a). Because of the ray path geometry and the large amplitude dominance of the source-side precursor, it is more difficult to observe scattered arrivals on the receiver-side of the path. Nonetheless several zones of scattering appear on the receiver-side beneath North America. The most pronounced of these zones are beneath (a) Northern Manitoba (Canada), (b) Saskatchewan (Canada), (c) North Dakota/Manitoba/Minnesota, (d) Wisconsin, and (e) Idaho/Utah (Figure 7b).

6. Discussion

6.1. Comparison to Synthetic Predictions

Using the PSVaxi technique we computed synthetic seismograms for a number of models with ULVZs, UHVZs, LLVPs, and CMB topography (additional synthetic model predictions are provided in Figures S17–S39 in Supporting Information S1). We analyzed these synthetic predictions using the automatic array analysis technique in the same way as the observations. In Figure 8, we show the synthetic predictions for the slowness of the scattered arrivals in time-distance space for the ULVZ and CMB topography models. An example of a UHVZ model is shown in Figure S31 in Supporting Information S1. We note that these synthetics are computed in a 2.5-D and not a 3-D geometry so all heterogeneity is located along the great circle path. This makes a direct comparison of travel-times with the observations not possible as some of the energy in the recorded data appears to come off the great-circle path. But currently a 2.5-D technique is the only viable option to calculate high-frequency synthetics for a large number of models. Nonetheless, these synthetic experiments allow us to make some general observations about the nature of the different types of heterogeneities we explored which can be used in the interpretation of these data.

When a ULVZ is on the path's source-side, we only observe PKP precursors in a limited epicentral distance range which depends on the ULVZ position as shown in Figure 8b. The pattern observed is concave downward and similar in shape regardless of where the ULVZ is placed along the path but the timing and distance range depends strongly on the location of the leftmost edge of the ULVZ (herein after referred to as the l_1 edge–model geometry is shown in the lower-right corner of Figure 8). For example, if the l_1 edge is located at 14° (Figure 8b), we only observe precursors in the distance range from ∼130° to 138° and the arrival time coincides with the minimum time for scatterers at the CMB only for a distance of 130°. When a ULVZ is on the path's receiver-side (Figure 8c), we observe PKP precursors that follow the approximate moveout of the CMB minimum time curve (i.e., they are convex in time vs. distance), but ULVZ location plays a key role in determining the arrival time and the range of epicentral distances where the arrivals occur as precursors despite the scatterers being located at the CMB. Note

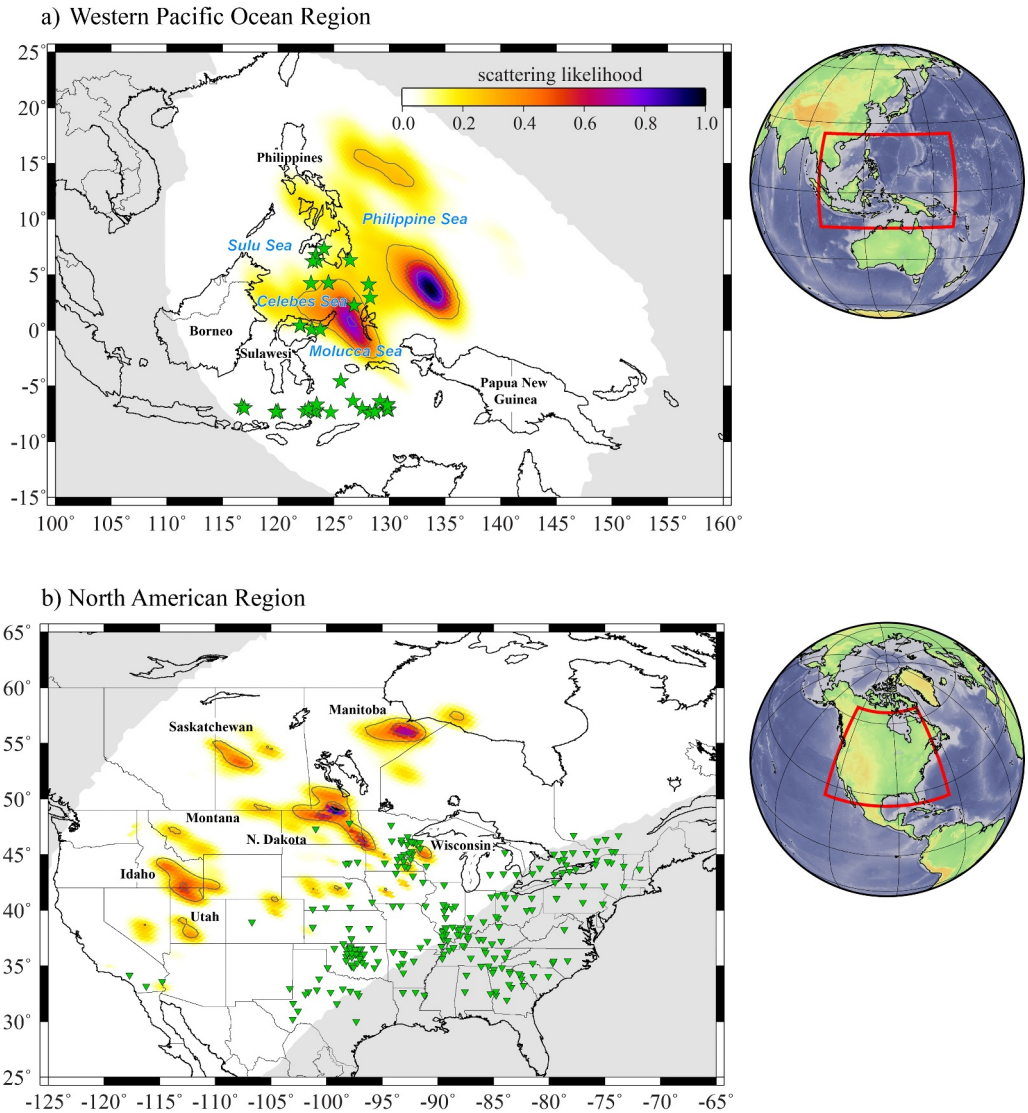

Figure 7. Scattering likelihood for (a) the western Pacific Ocean region (source side), and (b) North America (receiver side). Green stars show event locations and green triangles show array centroid locations where scattered arrivals were detected. Gray shaded areas show regions with no data coverage for PKP precursors.

that as the l_1 edge moves away from the source the arrival time gets later (closer to the PKIKP arrival) which is similar to the behavior shown for heterogeneity occurring at shallower depths in 1-D volumetric scattering models (e.g., Mancinelli & Shearer, 2013). In Figure 8d, we show results for four random realizations of CMB topography where the topography exists everywhere on the CMB. For these models the arrivals are dominated by receiver-side scattering which appear as convex curves, but in discontinuous segments depending on the location of the topographic highs and lows relative to source and receiver. For CMB topography models we see scatterers at all distances, with arrival times typically close to the CMB minimum time. The online supplements (Figures S35 and S36 in Supporting Information S1) also show an example where CMB topography is confined to the source-side. Again, we see segmented behavior with concave travel-time/distance behavior similar to that in Figure 8b for source-side heterogeneities, but the arrivals detected are closer to the CMB minimum time curves. Ultra-High Velocity Zone arrivals appear similar to ULVZ arrivals.

Simulations with two ULVZs in the velocity model are shown in Figure 8e (two source side ULVZs) and 8f (source and receiver side ULVZ). When two ULVZs are located on the source-side (Figure 8e), it is difficult for the automatic array processing technique to distinguish both of them at all distances. This is because the arrivals

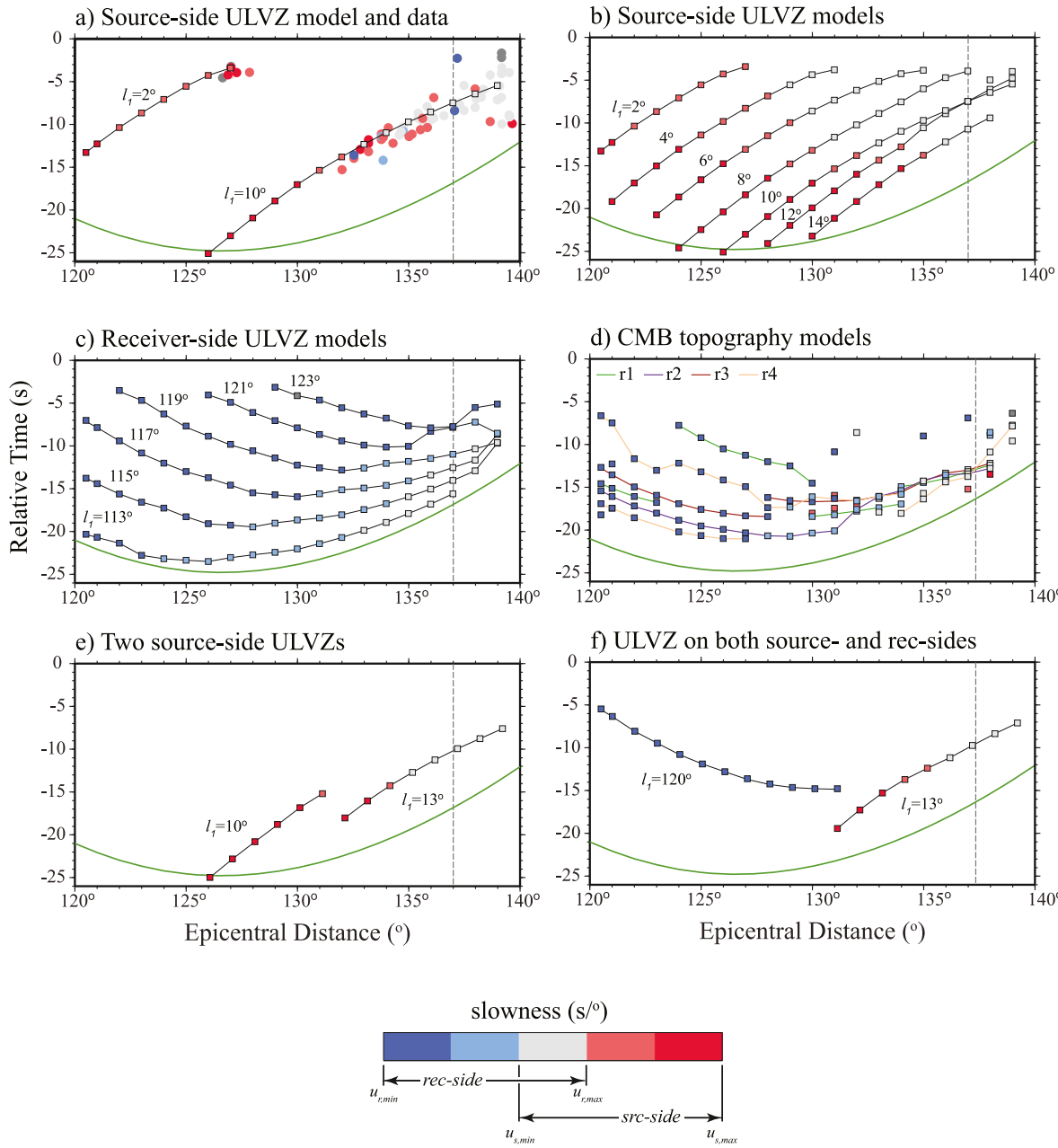

Figure 8. In each panel the scattered arrivals found with the automatic array processing technique are shown for synthetic models. In panel (a) the best fitting ultra-low velocity zone (ULVZ) models are overlain on observations for the 12 August 2013 (00:53) event. Models shown are for ULVZ models with $l_1 = 2°$ and $l_1 = 10°$. (b) Results for 7 models of source-side ULVZ heterogeneity with varying position from $l_1 = 2°–14°$. (c) Results for 6 models of receiver-side ULVZ heterogeneity with varying position from $l_1 = 113°–123°$. (d) Results for 4 random realizations of topography on the core-mantle boundary. (e) Results for two ULVZ models located on the source-side with $l_1 = 10°$ and $l_1 = 13°$. (f) Results when a ULVZ is on both the source and receiver sides of the path at $l_1 = 13°$ and $l_1 = 120°$. Slowness shading is the same as in Figure 1. A schematic of the ULVZ model definitions is shown in the lower right-hand corner for a position of $l_1 = 8°$ and a length (l) of 2.5°.

overlap in epicentral distance with almost identical slowness and the array processing approach is unable to identify the two arrivals with similar slowness. When a ULVZ is located on both the source- and receiver-sides (Figure 8f), the larger amplitude source-side ULVZ dominates the observations at the largest epicentral distances, but we are still able to observe the receiver-side ULVZ at shorter distances. If the receiver-side ULVZ is placed further away (e.g., at $l_1 = 123°$), there is greater separation in time between the source-side and receiver-side precursors and we are better able to detect the receiver-side precursors as well.

In Figure 8a, we show results from one event (12 Aug. 2013) in comparison to model results for ULVZs with l_1 edges at 2° and 10°. This event is chosen as its distance and azimuth distribution is representative of a large number of the events in our catalog that show a large amplitude precursor with concave time/distance behavior (source-side scattering). These synthetic predictions are remarkably similar to these observations suggesting a source-side scattering heterogeneity. We note that the actual observations show significant deviation in back-azimuth away from the great circle path, so a ULVZ edge at 10° as inferred from these 2.5-D synthetics is not in perfect agreement with the recorded data. However, the scattering analysis does indicate a scatterer at 2° angular distance right along the great circle path which is coincident with the grouping of observations between 126° and 127° distance. Nonetheless, compared to receiver-side or CMB topography scattering, the source-side ULVZ heterogeneity does a remarkable job at predicting the shape, timing, and slowness of the observations. It is possible that a UHVZ model produces similar well-fit predictions. But as discussed in the next section, previous studies using SPdKS and ScP seismic arrivals have identified ULVZs in this location. Hence, although we cannot necessarily rule out a UHVZ interpretation for these precursors, a ULVZ model is the preferred origin of this heterogeneity.

6.2. Relationship to Lower Mantle Features in the Western Pacific Ocean Region

The inferred scatterer locations (green contours) in relation to lower mantle tomography from model S40RTS (Ritsema et al., 2011) and ULVZ detections from other studies (He et al., 2006; Idehara, 2011; Pachhai et al., 2015; Thorne et al., 2020, 2021; Yao & Wen, 2014) are shown in Figure 9. Beneath the western Pacific Ocean region, the inferred scatterers are located near the boundary of the Pacific Large Low Velocity Province (LLVP). Several large ULVZs have previously been identified to be located in the immediate vicinity of our inferred scattering locations here as detected by (a) SPdKS (Jensen et al., 2013; Thorne et al., 2020, 2021) and (b) ScP postcursors (Idehara, 2011; Pachhai et al., 2015). Several previous studies have inferred that PKP energy is likely scattered from this region. Global studies have identified likely above average scattering in this region but have not separated out source-versus receiver-side scattering (Bataille & Flatté, 1988; Hedlin & Shearer, 2000; Ma & Thomas, 2020; Waszek et al., 2015) and thus have not uniquely identified this region as the source of the scattering. Nonetheless, a global study by Mancinelli et al. (2016) grouped precursors spatially by their PKIKP pierce points on the CMB, which were further subdivided into azimuthal bins, and compared the amplitudes of the precursory wavefield to global averages. Their analysis shows that PKP paths interacting with structure beneath the West Pacific and North America generally have larger precursor amplitudes and corroborates our findings here. A detailed study by Yao and Wen (2014) found evidence for scattering in this region as well, but indicated that the strongest scattering lies to the south and west of the Philippines, an area not sampled in our study. This study identified the cause of the scattering as being due to a ULVZ because the detected precursor amplitudes would require at least a 7%–10% δV_P contrast best explained through ULVZs but no detailed modeling was performed.

There are many factors that influence PKP precursor amplitudes that make it challenging to directly compare amplitudes in our synthetic experiments to data. For example, with the PSVaxi technique we calculate purely elastic synthetics without the effects of attenuation. The attenuation of the mantle and inner-core affect the relative amplitude ratios of PKP precursors to PKIKP (Mancinelli et al., 2016). Furthermore, differences in source radiation pattern are not included with the ring-source used in PSVaxi (Jahnke et al., 2008), but given the very similar take-off angles of PKP and PKIKP this likely has a minor effect. A major factor is that our calculations are done on a 2-D and not a 3-D grid. Comparison of synthetic seismograms computed for 2-D axisymmetric heterogeneities versus fully 3-D heterogeneities shows significant differences in the focusing and subsequent amplitudes of scattered arrivals (Krier et al., 2021) with larger magnitude velocity perturbations required for 3-D models to generate similar amplitude arrivals. However, 3-D calculations with attenuation at 1–2 s dominant periods are still computationally too expensive to conduct for more than a few models. Nonetheless, we measured amplitude ratios of the PKP precursor wavefield relative to PKIKP for 9 events that showed the most pronounced source-side scattering arrivals (see Figure S40 in Supporting Information S1). The amplitude ratios are distance dependent and start to grow from approximately zero at an epicentral distance of 127° to 0.1–0.5 around 135°–137°. Calculating the amplitude ratios from our synthetics, we find that we can match the precursor to PKP amplitude ratios with δV_P contrasts between −5 and −10%. Because the calculations are done for 2.5-D model geometries, this likely represents a lower bound on the velocity contrast, but points to the necessity of ULVZ-like heterogeneities to explain the amplitudes of the precursor arrivals.

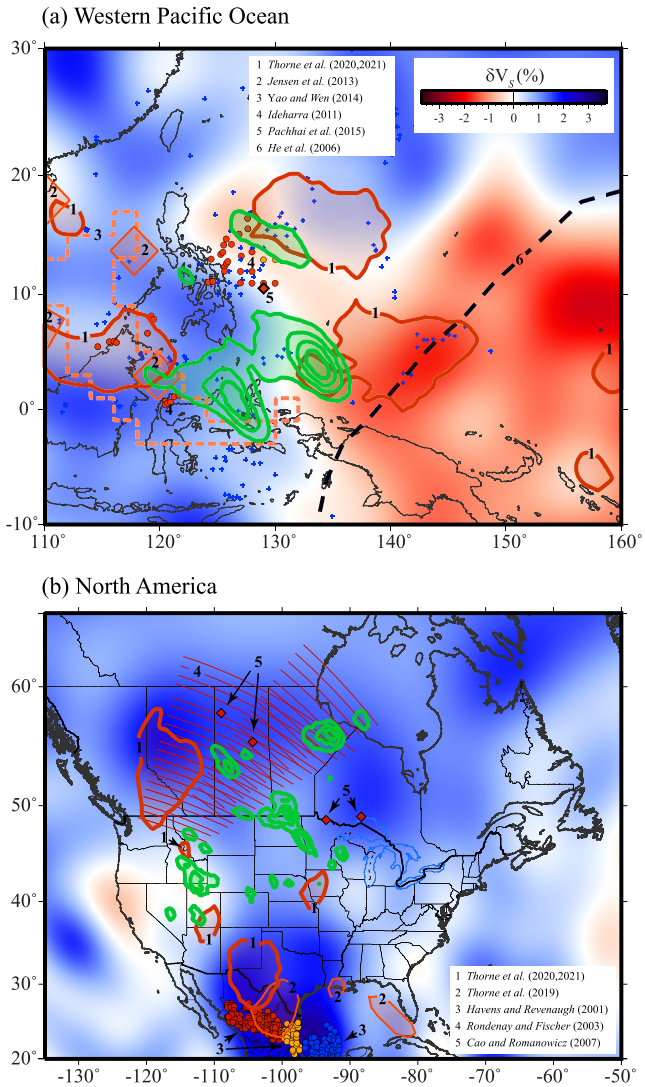

Figure 9. (a) Location of source-side PKP scatterers (contours drawn with heavy green lines) in relation to previous ultra-low velocity zone (ULVZ) detections. ULVZs shown are: (1) most parsimonious ULVZ locations using SPdKS are drawn with red lines (Thorne et al., 2020, 2021), (2) positive detections of ULVZs using SPdKS (Jensen et al., 2013), (3) ULVZ inferred from PKP scattering is shown with orange dashed lines (Yao & Wen, 2014), (4) red and orange circles show ScP bounce points for positive and possible ULVZ detections respectively, whereas blue crosses show non-detections of ULVZs using ScP (Idehara, 2011), (5) red diamond shows positive ULVZ detection (Pachhai et al., 2015), and (6) the black dashed line shows the sharp boundary in ScS-S travel-times inferred by (He et al., 2006). ULVZ structure is inferred in this study to lie to the northwest of this boundary. (b) Location of receiver-side PKP scatterers (contours drawn with heavy green lines) in relation to previous ULVZ and PKP precursor detections. Shown are: (1) most parsimonious ULVZ locations using SPdKS are drawn with red lines (Thorne et al., 2020, 2021), (2) highly anomalous SPdKS waveforms are drawn with thinner red lines (Thorne et al., 2019), (3) locations of ULVZs from PcP bounce points are drawn as circles (red = yes, blue = no, orange = maybe) (Havens & Revenaugh, 2001), (4) SPdKS paths where SKS postcursors have been detected (Rondenay & Fischer, 2003), and (5) locations of previous PKP precursors are shown with red diamonds (Cao & Romanowicz, 2007). Background in both panels is S-wave velocity perturbation from model S40RTS (Ritsema et al., 2011).

This region of the western Pacific lower mantle is, however, exceptionally complex. In addition to the inferred ULVZs, the western border of the Pacific LLVP lies here and has been shown to have sharp boundaries (He et al., 2006; Takeuchi et al., 2008). Scattering from sharp LLVP edges could contribute to the PKP precursor energy observed here, but LLVPs have been found to show only small δV_P variations on the order of 3% which are not able to explain the large amplitude precursors we observe here (see Figure S32 in Supporting Information S1). UHVZs are a possibility that fit the concave nature of the time/distance observations, but have thus far only tentatively been identified beneath Central America (Garnero et al., 2020; Yu, 2020) and there is currently no indication of their existence in this region. If UHVZ existence is established using other seismic phases, then future studies will need to further consider them as a possible source of PKP precursor energy. An inversion for CMB topography using PKP arrivals indicate as much as 4 km in topographic relief in this location (Sze & van der Hilst, 2003). But the same study shows no topography when using only PcP. Because PcP does not have source-/receiver-side ambiguity, this puts the topography in this location in question. Furthermore a detailed study using P4KP-PcP travel-times shows almost no CMB topography in this region (Tanaka, 2010). Our precursor detections occur later in time than the predictions for our models of CMB topography. However, we cannot rule out singular topographic highs which could produce precursors similar in appearance to ULVZs (see Figure S37 in Supporting Information S1). Nevertheless, the lack of topographic relief inferred from PcP argues against a topographic origin to these precursors.

Given the independent evidence that ULVZs exist in this region (from SPdKS and ScP studies), the outstanding agreement of our array observations with ULVZ synthetic predictions, and the necessity for large velocity contrasts to explain the precursors amplitudes, we propose that the large amplitude precursor we observe in the majority of our data are best explained by ULVZs coalescing against the western margin of the Pacific LLVP. Nonetheless we do not have perfect agreement between the broad scattering zone we observe here and the locations of known ULVZs. Part of this may be due to the difficulty in detecting ULVZs with short period ScP arrivals. Recent efforts indicate that 2- and 3-D ULVZ morphology may complicate ULVZ detection with ScP because additional arrivals exist even when ScP does not directly strike the ULVZ from above (Pachhai et al., 2023). There are also challenges in locating ULVZs with the SPdKS phase. In the likelihood maps of Thorne et al. (2021), which are shown in Figure 9, the ULVZ is presumed to be along the Pd segment on the CMB but determining the exact ULVZ placement requires detailed waveform modeling for each ULVZ which was beyond the scope of Thorne et al. (2021). The true ULVZ landscape in this region is at present unknown, but as can be seen in Figure 9 there is a preponderance of evidence that ULVZs do exist here, and the small-scale details of where they do and do not exist in this area is as yet to be determined.

6.3. Relationship to Lower Mantle Feature Beneath North America

The scattering locations beneath North America do not overlay known ULVZ features like they do in the Pacific. In part this may be due to our lack of knowledge of ULVZs in this region, as ULVZ sensitive phases are not as commonly observed here, or if they are, such as receiver-side SKPdS, anomalous waveforms are not as easily identified (Thorne et al., 2021). The exception is that SKS post-cursors have been identified and modeled as being due to ULVZs beneath western Canada (Rondenay & Fischer, 2003) in areas

that also coincide with some of our scattering locations. Nevertheless, the scattering locations we infer in this study do not readily align with known features and appear more spread out across the CMB. There is an appearance that they may also be smaller-scale, but this may just reflect the difficulty in detecting precursors originating here, as the large amplitude source-side precursors dominate the wavefield. Nevertheless, the scattering region detected beneath the North Dakota area of North America is comparable in size to those beneath the western Pacific Ocean (in the range from 7° to 9° or ∼425–550 km on the CMB).

Measuring amplitude ratios for precursors generated beneath North America is challenging. Distinct receiver-side precursors cannot readily be identified in the event stacks the same way as they can for the source-side precursors, but we can identify distinct precursors in distance profiles that are plotted in narrow azimuthal windows. Again, naively calculating amplitude ratios from our synthetic seismograms and comparing to amplitude ratios from 7 events where we identify receiver-side precursors, this suggests that δV_P reductions of 10% are likely too large, but reductions between 5% and 7.5% are plausible (Figure S41 in Supporting Information S1). Again, these velocity contrasts may be underestimated because the calculations were done in 2.5-D. These P-wave velocity reductions appear to be of similar magnitude as those on the source-side, which could also imply a ULVZ origin.

6.4. Ultra-Low Velocity Zone Origins

ULVZs located exterior to and at the edges of the LLVPs have been suggested to be caused by compositional heterogeneities (Li et al., 2017; McNamara et al., 2010). One source of such compositional heterogeneities belongs to subducted oceanic crust (Hansen et al., 2023; Li, 2023; Tackley, 2011). Oceanic crust is primarily made of MORB with a small fraction of sediments. MORB is intrinsically denser than the background pyrolitic mantle at most mantle depths (Hirose et al., 2005; Ringwood & Irifune, 1988; Tsuchiya, 2011). Once being subducted to the lowermost mantle, the intrinsically dense subducted MORB could segregate from cold subducted slabs and accumulate on the CMB (Christensen & Hofmann, 1994; Jones et al., 2020; Li, 2023; Li & McNamara, 2022; Tackley, 2011). Mineral physics experiments have found that MORB has a low melting temperature and thus could be partially molten at the CMB (Andrault et al., 2014, 2017; Pradhan et al., 2015). Here, we interpret the ULVZs in the lowermost mantle beneath the western Pacific Ocean and North America as possibly caused by molten MORB. The reasoning of this interpretation is elaborated as follows.

First of all, both of our seismic imaging regions beneath western Pacific Ocean and North America are located outside of the LLVPs. We calculated the present-day instantaneous mantle flow field by converting the S-wave velocity anomaly from tomography model S40RTS (Ritsema et al., 2011) to density anomaly. Details about the model are presented in the Online Supplements. We find that, on a global scale, mantle flow in the D″ layer moves from downwelling centers toward the two LLVPs (Figure 10a). Specifically, the seismic study region beneath the western Pacific is slightly displaced from downwelling centers, and the mantle flow moves laterally toward the Pacific LLVP, but the region beneath North America is right in the downwelling centers and is characterized by divergent lateral mantle flow (Figure 10a). Similar global features of D″ flow have also been predicted in other geodynamic modeling studies that use different model parameters (Steinberger & Holme, 2008; Walker et al., 2011; Yoshida, 2008). Because these two regions are adjacent to and in large part likely include relatively cold subducted slab material, they are expected to have a relatively low temperature. Therefore, the formation of ULVZs in these regions likely requires the contribution of chemical heterogeneities.

One source of chemical heterogeneities outside the LLVPs belongs to the subducted materials. Recently, Hansen et al. (2023) computed global convection models in which the large-scale convection pattern is guided by the surface plate motion history in the past 200 Myr. They used passive tracers to track the advection of subducted materials in the deep mantle and showed that most regions on the CMB, except the interiors of the LLVPs, are covered by subducted materials which have sunk to the deep mantle over the past 200 Myr. Our two seismic study regions are also predicted to be covered by subducted materials (Figure 10b).

However, the models of Hansen et al. (2023) did not consider segregation of subducted oceanic crust from subducted slabs in the lowermost mantle. We therefore computed a new model to demonstrate this possibility. The model setup is the same as the reference model (Case 1) in Li (2023) which is a 3-D spherical box model featured by single-sided subduction of oceanic crust to the deep interior. The layer of oceanic crust is 10-km-thick and 2% intrinsically denser than the background. Different from the model in Li (2023), our new model also includes a layer of intrinsically dense primordial material in the lowermost mantle at the beginning of the calculation. Details of model setup are provided in Li (2023) and in the Online Supplements. Shortly after the

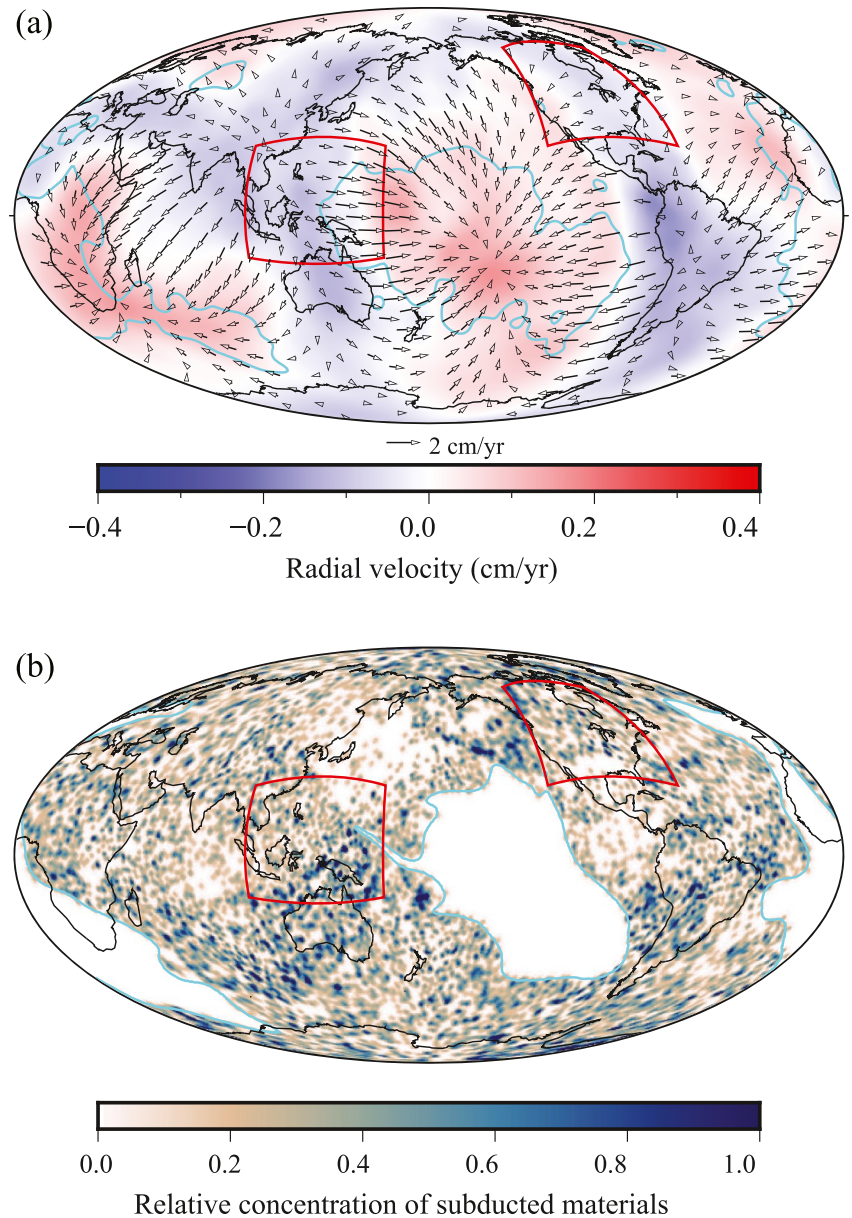

Figure 10. (a) Present-day mantle flow velocities at 2,800 km depth based on geodynamic calculations. Cyan contours show S-wave velocity anomaly at −0.5% from the S40RTS tomography model (Ritsema et al., 2011). (b) Present-day distribution of subducted materials in the lowermost 100 km of the mantle after 200 Myr of subduction history based on a geodynamic simulation. The cyan contours show the boundaries of thermochemical piles that represent LLVPs. The red boxes in panels (a, b) show the seismic study regions beneath the western Pacific and North America, respectively as outlined in Figure 7.

initiation of the calculation, the primordial material is pushed aside after the arrival of the subducted slab in the lowermost mantle, forming thermochemical piles (e.g., Figures 11a, 11c, and 11e) that could represent the seismically observed LLVPs. The subducted oceanic crust in the lowermost mantle episodically segregates from the slab and falls to the CMB (Figure 11). The segregated crust then migrates laterally along the CMB from regions beneath subduction toward the edges of the thermochemical piles (Figure 11). As a result, the distribution of subducted oceanic crust is time-dependent, and could be distributed across all regions exterior to and at the edges of the piles.

However, the P-wave velocity perturbations of solid MORB is predicted to only be on the order of 1%–2% or less (Wang et al., 2020); therefore, solid MORB itself does not explain strong scattering observed in this study. One

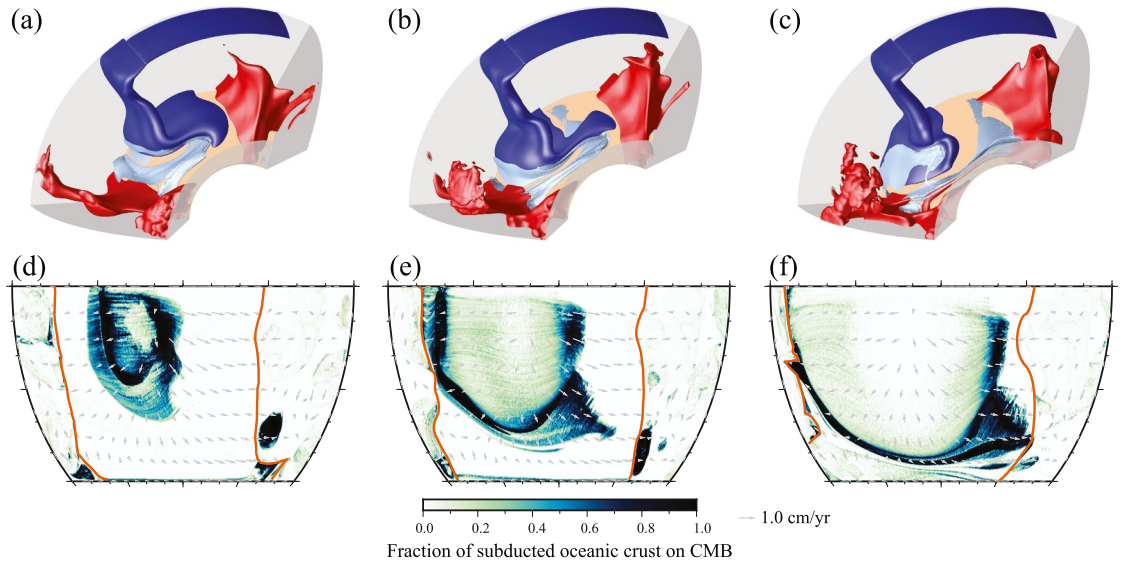

Figure 11. (a–c). Snapshots of the temperature and compositional field from a regional 3-D geodynamic model at 2,742 Myr (a), 2,865 Myr (b), and 3,024 Myr (c) after the initial condition. Dark blue colors show subducted slabs, red colors show regions that consist of thermochemical piles in the lowermost mantle and upwelling plumes on top of the piles, and the silver colors show subducted oceanic crust in the D" layer. (d–f), the corresponding fraction of subducted oceanic crust at the core-mantle boundary (CMB) at 2,742 Myr (d), 2,865 Myr (e), and 3,024 Myr (f). Gray arrows show mantle flow velocities at the CMB, which diverge away from regions beneath subduction toward the thermochemical piles at the east and west side boundaries. The orange curves show the edges of thermochemical piles that represent the LLVPs.

important feature of MORB is that its melting temperature is lower than the CMB temperature (Andrault et al., 2014; Hirose et al., 1999; Pradhan et al., 2015), so it may be partially molten on the CMB. The presence of hot thermal anomalies due to small-scale convection outside the LLVPs (Li, 2020) can additionally promote the melting of the crustal materials above the CMB. Once partially molten, melts could either drain out of or be trapped within the solid matrix depending on the melt fraction, physical properties of melts (density, viscosity, permeability) and the strength of background viscous coupling (Dannberg et al., 2021; Hernlund & Jellinek, 2010). If melts are suspended in the matrix due to a variety of possibilities such as low melt fraction, low permeability, low melt density anomaly, high melt viscosity, and/or high viscous coupling, a 10% and 30% P- and S-wave velocity reduction respectively can be explained by about 5%–30% of partial melting depending on the geometry of melts (Williams & Garnero, 1996). In this sense, our results suggest that the ULVZ scatterers beneath the western Pacific (which are at the edges of the Pacific LLVP) and beneath North America (which is right beneath subduction regions) may both be explained by the same origin of partially molten MORB in the subducted oceanic crust.

Other sources of compositional heterogeneities on the CMB include remnants of crystallization of a basal magma ocean (Labrosse et al., 2007) and products of core-mantle reaction (Manga & Jeanloz, 1996; Otsuka & Karato, 2012). Similar to subducted oceanic crust, these materials can also accumulate at the edges of the LLVPs and also contribute to the ULVZ scatterers observed beneath the western Pacific. However, it may be difficult to explain the ULVZ scatterers beneath North America with either of these models. Remnants of a basal magma ocean may have long been advected to the LLVP regions after Earth's long mantle convection history (Pachhai et al., 2022). Products of core-mantle reaction, once produced, may also be advected toward the LLVPs and it remains an open question whether sufficient volume of such materials can be made by core-mantle reaction before they are advected outside of regions beneath subduction.

The interpretation of the origin of ULVZs in our study regions is summarized in a cartoon shown in Figure 12. When subducted slabs approach the lowermost mantle, pre-existing chemical heterogeneities on the CMB (such as remnants of magma ocean, primordial materials, products of CMB reactions) are pushed toward the edges of LLVPs (Figure 12a). As subducted slabs reach the base of the mantle, the subducted oceanic crust segregates on the CMB and is partially molten (Figure 12b). Oceanic crust at the CMB migrates laterally along the CMB,

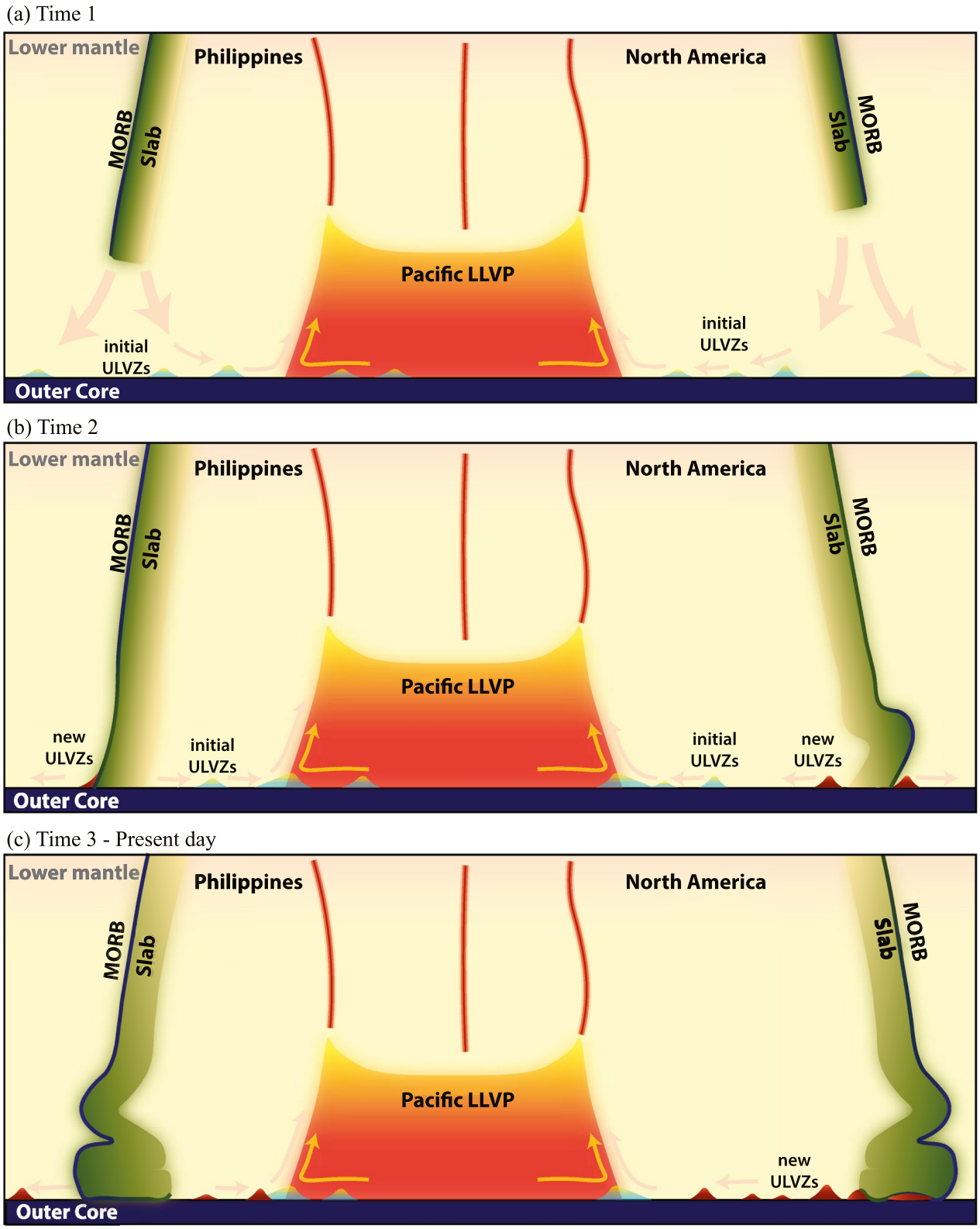

Figure 12. Cartoon depicting evolution of ULVZs in the lower mantle. Lithospheric slabs are shown in green and topped by blue mid-ocean ridge basalt (MORB) material. The Pacific Large Low Velocity Province is shown in orange. Older ULVZs generated by mechanisms such as core-mantle reactions, primordial remnants, and older subduction are shown in light blue. Newly created ULVZs by melting of MORB are shown in red. Three different stages of evolution are shown (a) before recent subduction beneath North America and the Philippines reaches the core-mantle boundary (CMB), (b) when subduction reaches the CMB, and (c) the present day.

toward the edges of the LLVPs, whereas molten pockets of MORB in the oceanic crust beneath the western Pacific Ocean already reach the LLVPs' margins. Because the downwelling centers beneath North America are further away from the LLVP boundary, the molten pockets of MORB beneath North America are still advecting toward the LLVPs (Figure 12c). Therefore, ULVZs beneath western Pacific Ocean and North America could be explained by single mechanism of molten MORB. But ULVZs in the western Pacific region could be a combination of materials from multiple different sources.

If ULVZs are generated by the partial melting of MORB near subduction zones, then large amplitude PKP precursors should be observable in regions where subducted lithosphere is impinging on the CMB. Our geodynamic simulation (Figure 10b) suggests that two locations worth further investigation are beneath the central part of South America, and the region beneath New Guinea extending down through Australia. For the first region, central South America, there is evidence for ULVZ existence (Thorne et al., 2020, 2021). But searches for PKP precursors show heterogeneous results, with one study not showing elevated amplitudes of PKP precursors for events originating in South America (Mancinelli et al., 2016), but other studies indicate PKP precursors (Hedlin & Shearer, 2000; Ma & Thomas, 2020; Waszek et al., 2015). It is possible that this region is highly heterogeneous, similar to the region we investigate beneath the Western Pacific. With the large number of events occurring in South America, this could be an excellent target area to search for additional source-side PKP precursors. The second region, from New Guinea down through central Australia, currently shows no ULVZ evidence, but is not well situated to be probed with standard seismic phases used in hunting ULVZs (Yu & Garnero, 2018). However, some evidence of PKP precursors originating here has been put forth (Ma & Thomas, 2020; Mancinelli et al., 2016; Waszek et al., 2015). Again, precursor observations for this region appear highly heterogeneous, but earthquakes from the Java trench could illuminate additional source-side PKP scattering that could potentially be used to identify previously unknown ULVZ structure beneath Australia.

7. Conclusions

In this study we have made a new analysis of PKP precursor arrivals using 2.5-D synthetic waveform predictions and advances in seismic array processing. The largest pre-cursor arrivals we analyzed in this study showed a travel-time moveout pattern that is unique to scatterers located on the source-side of the path. The distinction between source- and receiver-side travel-time moveouts has not been presented in previous studies and may be highly diagnostic of scatterer location. Even though these precursor arrivals don't arrive at the minimum CMB time utilized in 1-D modeling efforts, a CMB origin is still consistent with these data because lateral variations in seismic heterogeneity position can also account for the same arrival times. Our observations are consistent in slowness, time, and backazimuth with a CMB origin, but synthetic experiments suggest that it would be difficult to determine if the scatterers were directly on the CMB or just within the lowermost 10–20 km of mantle. These scatterers require large (5%–15%) P-wave velocity contrasts and ULVZs are the only known lower mantle features at present in which such large contrasts have been identified. Evidence from other seismic phases such as SPdKS require a CMB origin to ULVZs (e.g., Garnero & Helmberger, 1995) and increases in ULVZ density from ScP studies (e.g., Rost et al., 2006) also supports ULVZs directly on top of the CMB. This is not to say that scatterers do not exist above the CMB as suggested in previous studies of PKP precursors (e.g., Mancinelli & Shearer, 2013). Rather a good explanation for the largest amplitude scatterers we observe in this study is that they originate from the CMB. The features responsible for these large amplitude precursor arrivals could be embedded in a D″ region that contains heterogeneity at a range of spatial scales (Cormier, 2000).

If ULVZs are indeed generating the scattering energy, we suggest that MORB melting is an excellent candidate for explaining their presence in both the western Pacific Ocean region and beneath North America. Other sources of ULVZ genesis could contribute to the creation of ULVZ material. For example, in the early Earth ULVZs could have been created through the crystallization of a magma ocean. Or over the 4.5-billion-year history of the Earth significant core-mantle reaction products could have accumulated. But geodynamic modeling implies that both ULVZ sources should have been advected to LLVP margins, or to regions of upwelling within 100–200 million years. ULVZs in the western Pacific Ocean next to the Pacific LLVP may indeed include ULVZ material from these different sources. But it is challenging to explain the ULVZs beneath North America, and other subduction settings (e.g., Festin et al., 2024; Thorne et al., 2019; Wolf et al., 2024) by such mechanisms. A recent global study of ULVZ distribution suggests that as large as 19.7% of the CMB area may contain ULVZ material and that these materials are distributed among all CMB provinces (Thorne et al., 2021). Because ULVZs are likely advected across the CMB region rapidly, a source to generate them as rapidly is also required to explain their presence in

downwelling regions. A subduction related source supplying MORB material, which may undergo subsequent melting, to the CMB may be a leading candidate for such ULVZ generation. Future geodynamic and mineral physics experiments are required to test the rate at which ULVZs can be produced in such a manner.

Conflict of Interest

The authors declare no conflicts of interest relevant to this study.

Data Availability Statement

All seismic recordings used in this study are stored and shared at the University of Utah's hive data repository (Thorne, 2024).

Acknowledgments
The authors acknowledge the University of Utah Center for High Performance Computing (CHPC) for computing resources and support. We thank Editor Thorsten Becker, Vernon Cormier, and two anonymous reviewers for their thoughtful suggestions which helped improve this manuscript. MT and SP were partially supported by NSF Grants EAR-1723081 and EAR-2139966. ML was partially supported by EAR-2216564. JW was supported by NERC large grant Mantle Circulation Constrained NE/T012684/1 and SR was partially supported by NERC Grant NE/R012199/1. The facilities of IRIS Data Services, and specifically the IRIS Data Management Center, were used for access to waveforms, related metadata, and/or derived products used in this study. IRIS Data Services are funded through the Seismological Facilities for the Advancement of Geoscience (SAGE) Award of the National Science Foundation under Cooperative Support Agreement EAR-1851048.

References

Andrault, D., Bolfan-Casanova, N., Bouhifd, M. A., Boujibar, A., Garbarino, G., Manthilake, G., et al. (2017). Toward a coherent model for the melting behavior of the deep Earth's mantle. *Physics of the Earth and Planetary Interiors*, *265*, 67–81. https://doi.org/10.1016/j.pepi.2017.02.009

Andrault, D., Pesce, G., Bouhifd, M. A., Bolfan-Casanova, N., Hénot, J.-M., & Mezouar, M. (2014). Melting of subducted basalt at the core-mantle boundary. *Science*, *344*(6186), 892–895. https://doi.org/10.1126/science.1250466

Bataille, K., & Flatté, S. M. (1988). Inhomogeneities near the core-mantle boundary inferred from short-period scattered PKP waves recorded at the global digital seismograph network. *Journal of Geophysical Research*, *93*(B12), 15057–15064. https://doi.org/10.1029/jb093ib12p15057

Bataille, K., Wu, R.-S., & Flatté, S. M. (1990). Inhomogeneities near the core-mantle boundary evidenced from scattered waves: A Review. *Pure and Applied Geopysics*, *132*(1/2), 151–173. https://doi.org/10.1007/bf00874361

Bolt, B. A. (1962). Gutenberg's early PKP observations. *Nature*, *196*(4850), 122–124. https://doi.org/10.1038/196122a0

Buchbinder, G. G. R. (1974). Diffraction from the PKP caustic B. *Bulletin of the Seismological Society of America*, *64*(1), 33–43. https://doi.org/10.1785/bssa0640010033

Cao, A., & Romanowicz, B. (2007). Locating scatterers in the mantle using array analysis of PKP precursors from an earthquake doublet. *Earth and Planetary Science Letters*, *255*(1–2), 22–31. https://doi.org/10.1016/j.epsl.2006.12.002

Christensen, U. R., & Hofmann, A. W. (1994). Segregation of subducted oceanic crust in the convecting mantle. *Journal of Geophysical Research*, *99*(B10), 19867–819884. https://doi.org/10.1029/93JB03403

Cormier, V. F. (2000). D" as a transition in the heterogeneity spectrum of the lowermost mantle. *Journal of Geophysical Research*, *105*(B7), 16193–16205. https://doi.org/10.1029/2000jb900141

Crotwell, H. P., Owens, T. J., & Ritsema, J. (1999). The TauP Toolkit: Flexible seismic travel-time and ray-path utilities. *Seismological Research Letters*, *70*(2), 154–160. https://doi.org/10.1785/gssrl.70.2.154

Dannberg, J., Myhill, R., Grassmöller, R., & Cottaar, S. (2021). The morphology, evolution and seismic visibility of partial melt at the core-mantle boundary: Implications for ULVZs. *Geophysical Journal International*, *227*(2), 1028–1059. https://doi.org/10.1093/gji/ggab242

Doornbos, D. J. (1976). Characteristics of lower mantle inhomogeneities from scattered waves. *Geophysical Journal of the Royal Astronomical Society*, *44*(2), 447–470. https://doi.org/10.1111/j.1365-246X.1976.tb03667.x

Dziewonski, A. M., & Anderson, D. L. (1981). Preliminary reference Earth model. *Physics of the Earth and Planetary Interiors*, *25*(4), 297–356. https://doi.org/10.1016/0031-9201(81)90046-7

Ester, M., Kriegel, H.-P., Sander, J., & Xu, X. (1996). A density-based algorithm for discovering clusters in large spatial databases with noise. In E. Simoudis, J. Han, & U. M. Fayyad (Eds.), *Proceedings of 2nd international conference on knowledge discovery and data mining (KDD-96)* (pp. 226–231). AAAI Press.

Festin, M. M., Thorne, M. S., & Li, M. (2024). Evidence for ultra-low velocity zone genesis in downwelling subducted slabs at the core-mantle boundary. *The Seismic Record*, *4*(2), 111–120. https://doi.org/10.1785/0320240003

Frankel, A., & Clayton, R. W. (1986). Finite difference simulations of seismic scattering: Implications for the propagation of short-period seismic waves in the crust and models of crustal heterogeneity. *Journal of Geophysical Research*, *91*(B6), 6465–6489. https://doi.org/10.1029/jb091ib06p06465

Frost, D. A., Rost, S., Garnero, E. J., & Li, M. (2017). Seismic evidence for Earth's crusty deep mantle. *Earth and Planetary Science Letters*, *470*, 54–63. https://doi.org/10.1016/j.epsl.2017.04.036

Garnero, E., Yu, S., Shim, S.-H., Li, M., Ko, B., Thorne, M. S., & Zhao, C. (2020). Ultra high velocity zones at the core-mantle boundary. In *AGU fall meeting abstracts*.

Garnero, E. J., & Helmberger, D. V. (1995). A very slow basal layer underlying large-scale low-velocity anomalies in the lower mantle beneath the Pacific: Evidence from core phases. *Physics of the Earth and Planetary Interiors*, *91*(1–3), 161–176. https://doi.org/10.1016/0031-9201(95)03039-y

Garnero, E. J., Thorne, M. S., McNamara, A. K., & Rost, S. (2007). Fine-scale ultra-low velocity zone layering at the core-mantle boundary and superplumes. In D. A. Yuen, S. Maruyama, S.-i. Karato, & B. F. Windley (Eds.), *Superplumes: Beyond plate tectonics* (pp. 139–157). Springer.

Gutenberg, B. (1958). Caustics produced by waves through the Earth's core. *Geophysical Journal International*, *1*(3), 238–248. https://doi.org/10.1111/j.1365-246X.1958.tb00057.x

Haddon, R. A. W., & Cleary, J. R. (1974). Evidence for scattering of seismic PKP waves near the mantle-core boundary. *Physics of the Earth and Planetary Interiors*, *8*(3), 211–234. https://doi.org/10.1016/0031-9201(74)90088-0

Hansen, S. E., Garnero, E. J., Li, M., Shim, S.-H., & Rost, S. (2023). Globally distributed subducted materials along the Earth's core-mantle boundary: Implications for ultralow velocity zones. *Science Advances*, *9*(eadd4838), 1–11. https://doi.org/10.1126/sciadv.add4838

Haugland, S. M., Ritsema, J., van Keken, P. E., & Nissen-Meyer, T. (2018). Analysis of PKP scattering using mantle mixing simulations and axisymmetric 3D waveforms. *Physics of the Earth and Planetary Interiors*, *276*, 226–233. https://doi.org/10.1016/j.pepi.2017.04.001

Havens, E., & Revenaugh, J. (2001). A broadband seismic study of the lowermost mantle beneath Mexico: Constraints on ultralow velocity zone elasticity and density. *Journal of Geophysical Research*, *106*(B12), 30809–30820. https://doi.org/10.1029/2000JB000072

He, Y., Wen, L., & Zheng, T. (2006). Geographic boundary and shear wave velocity structure of the "Pacific anomaly" near the core–mantle boundary beneath western Pacific. *Earth and Planetary Science Letters*, *244*(1–2), 302–314. https://doi.org/10.1016/j.epsl.2006.02.007

Hedlin, M. A. H., & Shearer, P. M. (2000). An analysis of large-scale variations in small-scale mantle heterogeneity using Global Seismographic Network recordings of precursors to PKP. *Journal of Geophysical Research*, *105*(B6), 13655–613673. https://doi.org/10.1029/2000jb900019

Hedlin, M. A. H., Shearer, P. M., & Earle, P. S. (1997). Seismic evidence for small-scale heterogeneity throughout the Earth's mantle. *Nature*, *387*(6629), 145–150. https://doi.org/10.1038/387145a0

Hernlund, J. W., & Jellinek, A. M. (2010). Dynamics and structure of a stirred partially molten ultralow-velocity zone. *Earth and Planetary Science Letters*, *296*(1–2), 1–8. https://doi.org/10.1016/j.epsl.2010.04.027

Hirose, K., Fei, Y., Ma, Y., & Mao, H.-k. (1999). The fate of subducted basaltic crust in the Earth's lower mantle. *Nature*, *397*(6714), 53–56. https://doi.org/10.1038/16225

Hirose, K., Takafuji, N., Sata, N., & Ohishi, Y. (2005). Phase transition and density of subducted MORB crust in the lower mantle. *Earth and Planetary Science Letters*, *237*(1–2), 239–251. https://doi.org/10.1016/j.epsl.2005.06.035

Husebye, E. S., King, D. W., & Haddon, R. A. W. (1976). Precursors to PKIKP and seismic wave scattering near the mantle-core boundary. *Journal of Geophysical Research*, *81*(11), 1870–1882. https://doi.org/10.1029/JB081i011p01870

Idehara, K. (2011). Structural heterogeneity of an ultra-low-velocity zone beneath the Philippine Islands: Implications for core–mantle chemical interactions induced by massive partial melting at the bottom of the mantle. *Physics of the Earth and Planetary Interiors*, *184*(1–2), 80–90. https://doi.org/10.1016/j.pepi.2010.10.014

Jahnke, G. (2009). *Methods for seismic wave propagation on local and global scales with finite differences* (p. 99). Ludwig-Maximilians-Universität.

Jahnke, G., Thorne, M. S., Cochard, A., & Igel, H. (2008). Global SH-wave propagation using a parallel axisymmetric spherical finite-difference scheme: Application to whole mantle scattering. *Geophysical Journal International*, *173*(3), 815–826. https://doi.org/10.1111/j.1365-246X.2008.03744.x

Jensen, K. J., Thorne, M. S., & Rost, S. (2013). SPdKS analysis of ultralow-velocity zones beneath the western Pacific. *Geophysical Research Letters*, *40*(17), 1–5. https://doi.org/10.1002/grl.50877

Jones, T. D., Maguire, R. R., van Keken, P. E., Ritsema, J., & Koelemeijer, P. (2020). Subducted oceanic crust as the origin of seismically slow lower-mantle structures. *Progress in Earth and Planetary Science*, *7*(17), 17. https://doi.org/10.1186/s40645-020-00327-1

Kaneshima, S., & Helffrich, G. (1998). Detection of lower mantle scatterers northeast of the Marianna subduction zone using short-period array data. *Journal of Geophysical Research*, *103*(B3), 4825–4838. https://doi.org/10.1029/97jb02565

King, D. W., Haddon, R. A. W., & Cleary, J. R. (1974). Array analysis of precursors to PKIKP in the distance range 128° to 142°. *Geophysical Journal of the Royal Astronomical Society*, *37*(1), 157–173. https://doi.org/10.1111/j.1365-246x.1974.tb02450.x

Ko, B., Chariton, S., Prakapenka, V., Chen, B., Garnero, E. J., Li, M., & Shim, S.-H. (2022). Water-induced diamond formation at Earth's core-mantle boundary. *Geophysical Research Letters*, *49*(16), e2022GL098271. https://doi.org/10.1029/2022GL098271

Korenaga, J. (2013). Stacking with dual bootstrap resampling. *Geophysical Journal International*, *195*(3), 2023–2036. https://doi.org/10.1093/gji/ggt373

Krier, J., Thorne, M. S., Leng, K., & Nissen-Meyer, T. (2021). A compositional component to the Samoa ultralow-velocity zone revealed through 2- and 3-D waveform modeling of SKS and SKKS differential travel-times and amplitudes. *Journal of Geophysical Research: Solid Earth*, *126*(7), e2021JB021897. https://doi.org/10.1029/2021JB021897

Labrosse, S., Hernlund, J. W., & Coltice, N. (2007). A crystallizing dense magma ocean at the base of the Earth's mantle. *Nature*, *450*(7171), 866–869. https://doi.org/10.1038/nature06355

Lay, T., Hernlund, J. W., Garnero, E. J., & Thorne, M. S. (2006). A post-perovskite lens and D" heat flux beneath the central Pacific. *Science*, *314*(5803), 1272–1276. https://doi.org/10.1126/science.1133280

Li, M. (2020). The formation of hot thermal anomalies in cold subduction-influenced regions of Earth's lowermost mantle. *Journal of Geophysical Research: Solid Earth*, *125*(6), e2019JB019312. https://doi.org/10.1029/2019jb019312

Li, M. (2023). Variable distribution of subducted oceanic crust beneath subduction regions of the lowermost mantle. *Physics of the Earth and Planetary Interiors*, *341*(107063), 107063. https://doi.org/10.1016/j.pepi.2023.107063

Li, M., & McNamara, A. K. (2022). Evolving morphology of crustal accumulations in Earth's lowermost mantle. *Earth and Planetary Science Letters*, *577*(117265), 117265. https://doi.org/10.1016/j.epsl.2021.117265

Li, M., McNamara, A. K., Garnero, E. J., & Yu, S. (2017). Compositionally-distinct ultra-low velocity zones on Earth's core-mantle boundary. *Nature Communications*, *8*(177), 1–9. https://doi.org/10.1038/s41467-017-00219-x

Ma, X., Sun, X., & Thomas, C. (2019). Localized ultra-low velocity zones at the eastern boundary of Pacific LLSVP. *Earth and Planetary Science Letters*, *507*, 40–49. https://doi.org/10.1016/j.epsl.2018.11.037

Ma, X., Sun, X., Wiens, D. A., Wen, L., Nyblade, A., Anandakrishnan, S., et al. (2016). Strong seismic scatterers near the core-mantle boundary north of the Pacific Anomaly. *Physics of the Earth and Planetary Interiors*, *253*, 21–30. https://doi.org/10.1016/j.pepi.2016.01.007

Ma, X., & Thomas, C. (2020). Small-scale scattering heterogeneities in the lowermost mantle from a globaly analysis of PKP precursors. *Journal of Geophysical Research: Solid Earth*, *125*(3), e2019JB018736. https://doi.org/10.1029/2019JB018736

Mancinelli, N. J., Shearer, P., & Thomas, C. (2016). On the frequency dependence and spatial coherence of PKP precursor amplitudes. *Journal of Geophysical Research: Solid Earth*, *121*(3), 1873–1889. https://doi.org/10.1002/2015JB012768

Mancinelli, N. J., & Shearer, P. M. (2013). Reconciling discrepancies among estimates of small-scale mantle heterogeneity from *PKP* precursors. *Geophysical Journal International*, *195*(3), 1721–1729. https://doi.org/10.1093/gji/ggt319

Manga, M., & Jeanloz, R. (1996). Implications of a metal-bearing chemical boundary layer in D" for mantle dynamics. *Geophysical Research Letters*, *23*(22), 3091–3094. https://doi.org/10.1029/96gl03021

Margerin, L., & Nolet, G. (2003a). Multiple scattering of high-frequency seismic waves in the deep Earth: Modeling and numerical examples. *Journal of Geophysical Research*, *108*(B5), 2234. https://doi.org/10.1029/2002JB001974

Margerin, L., & Nolet, G. (2003b). Multiple scattering of high-frequency seismic waves in the deep Earth: *PKP* precursor analysis and inversion for mantle granularity. *Journal of Geophysical Research*, *108*(B11). https://doi.org/10.1029/2003JB002455

McNamara, A. K., Garnero, E. J., & Rost, S. (2010). Tracking deep mantle reservoirs with ultra-low velocity zones. *Earth and Planetary Science Letters*, *299*(1–2), 1–9. https://doi.org/10.1016/j.epsl.2010.07.042

Murakami, M., Sinogeikin, S. V., Hellwig, H., Bass, J. D., & Li, J. (2007). Sound velocity of $MgSiO_3$ perovskite to Mbar pressure. *Earth and Planetary Science Letters*, *256*(1–2), 47–54. https://doi.org/10.1016/j.epsl.2007.01.011

Otsuka, K., & Karato, S.-I. (2012). Deep penetration of molten iron into the mantle caused by a morphological instability. *Nature*, *429*(7428), 243–246. https://doi.org/10.1038/nature11663

Pachhai, S., Dettmer, J., & Tkalčić, H. (2015). Ultra-low velocity zones beneath the Philippine and Tasman Seas revealed by a trans-dimensional Bayesian waveform inversion. *Geophysical Journal International*, *203*(2), 1302–1318. https://doi.org/10.1093/gji/ggv368

Pachhai, S., Li, M., Thorne, M. S., Dettmer, J., & Tkalčić, H. (2022). Internal structure of ultralow-velocity zones consistent with origin from a basal magma ocean. *Nature Geoscience*, *15*(1), 79–84. https://doi.org/10.1038/s41561-021-00871-5

Pachhai, S., Thorne, M. S., & Rost, S. (2023). Improved characterization of ultralow-velocity zones through advances in Bayesian inference of ScP waveforms. *Journal of Geophysical Research: Solid Earth*, *128*(6). https://doi.org/10.1029/2023JB026415

Pradhan, G. K., Fiquet, G., Siebert, J., Auzende, A.-L., Morard, G., Antonangeli, D., & Garbarino, G. (2015). Melting of MORB at core-mantle boundary. *Earth and Planetary Science Letters*, *431*, 247–255. https://doi.org/10.1016/j.epsl.2015.09.034

Ringwood, A. E., & Irifune, T. (1988). Nature of the 650-km seismic discontinuity: Implications for mantle dynamics and differentiation. *Nature*, *331*(6152), 131–136. https://doi.org/10.1038/331131a0

Ritsema, J., Deuss, A., van Heijst, H.-J., & Woodhouse, J. H. (2011). S40RTS: A degree-40 shear-velocity model for the mantle from new Rayleigh wave dispersion, teleseismic traveltime and normal-mode splitting function measurements. *Geophysical Journal International*, *184*(3), 1223–1236. https://doi.org/10.1111/j.1365-246X.2010.04884.x

Rondenay, S., & Fischer, K. M. (2003). Constraints on localized core-mantle boundary structure from multichannel, broadband SKS coda analysis. *Journal of Geophysical Research*, *108*(B11). https://doi.org/10.1029/2003JB002518

Rost, S., Garnero, E. J., & Williams, Q. (2006). Fine-scale ultralow-velocity zone structure from high-frequency seismic array data. *Journal of Geophysical Research*, *111*(B09310). https://doi.org/10.1029/2005JB004088

Rost, S., & Thomas, C. (2002). Array Seismology: Methods and applications. *Reviews of Geophysics*, *40*(3). https://doi.org/10.1029/2000RG000100

Schlittenhardt, J. (1996). Array analysis of core-phase caustic signals from underground nuclear explosions: Discrimination of closely spaced explosions. *Bulletin of the Seismological Society of America*, *86*(1A), 159–171. https://doi.org/10.1785/bssa08601a0159

Shearer, P. M. (2007). Deep Earth structure–Seismic scattering in the deep Earth. *Treatise on Geophysics*, *1*, 695–729. https://doi.org/10.1016/b978-044452748-6.00021-3

Shearer, P. M., & Earle, P. S. (2004). The global short-period wavefield modelled with a Monte Carlo seismic phonon method. *Geophysical Journal International*, *158*(3), 1103–1117. https://doi.org/10.1111/j.1365-246X.2004.02378.x

Steinberger, B., & Holme, R. (2008). Mantle flow models with core-mantle boundary constraints and chemical heterogeneities in the lowermost mantle. *Journal of Geophysical Research*, *113*(B05403). https://doi.org/10.1029/2007JB005080

Swinbank, R., & Purser, R. J. (2006). Fibonacci grids: A novel approach to global modelling. *The Quarterly Journal of the Royal Meteorological Society*, *132*(619), 1769–1793. https://doi.org/10.1256/qj.05.227

Sze, E. K. M., & van der Hilst, R. D. (2003). Core mantle boundary topography from short period PcP, PKP, and PKKP data. *Physics of the Earth and Planetary Interiors*, *135*(1), 27–46. https://doi.org/10.1016/s0031-9201(02)00204-2

Tackley, P. J. (2011). Living dead slabs in 3-D: The dynamics of compositionally-stratified slabs entering a "slab graveyard" above the core-mantle boundary. *Physics of the Earth and Planetary Interiors*, *188*(3–4), 150–162. https://doi.org/10.1016/j.pepi.2011.04.013

Takeuchi, N., Morita, Y., Xuyen, N. D., & Zung, N. Q. (2008). Extent of the low-velocity region in the lowermost mantle beneath the western Pacific detected by the Vietnamese Broadband Seismograph Array. *Geophysical Research Letters*, *35*(L05307), 1–5. https://doi.org/10.1029/2008GL033197

Tanaka, S. (2010). Constraints on the core-mantle boundary topography from P4KP-PcP differential travel times. *Journal of Geophysical Research*, *115*(B04310). https://doi.org/10.1029/2009JB006563

Thomas, C., Kendall, J.-M., & Helffrich, G. (2009). Probing two low-velocity regions with *PKP* b-caustic amplitudes and scattering. *Geophysical Journal International*, *178*(1), 503–512. https://doi.org/10.1111/j.1365-246X.2009.04189.x

Thorne, M. S. (2024). Data for: Investigating ultra-low velocity zones as sources of PKP scattering beneath North America and the western Pacific Ocean: Potential links to subducted oceanic crust [Data] -The Hive. *University of Utah Research Data Repository*. https://doi.org/10.7278/S5d-d24y-bqdz

Thorne, M. S., & Garnero, E. J. (2004). Inferences on ultralow-velocity zone structure from a global analysis of SPdKS waves. *Journal of Geophysical Research*, *109*(B8). https://doi.org/10.1029/2004JB003010

Thorne, M. S., Garnero, E. J., Jahnke, G., Igel, H., & McNamara, A. K. (2013). Mega ultra low velocity zone and mantle flow. *Earth and Planetary Science Letters*, *364*, 59–67. https://doi.org/10.1016/j.epsl.2012.12.034

Thorne, M. S., Leng, K., Pachhai, S., Rost, S., Wicks, C. W., & Nissen-Meyer, T. (2021). The most parsimonious ultralow-velocity zone distribution from highly anomalous SPdKS waveforms. *Geochemistry, Geophysics, Geosystems*, *22*(1). https://doi.org/10.1029/2020GC009467

Thorne, M. S., Pachhai, S., Leng, K., Wicks, J. K., & Nissen-Meyer, T. (2020). New candidate ultralow-velocity zone locations from highly anomalous SPdKS waveforms. *Minerals*, *10*(211), 1–26. https://doi.org/10.3390/min10030211

Thorne, M. S., Takeuchi, N., & Shiomi, K. (2019). Melting at the edge of a slab in the deepest mantle. *Geophysical Research Letters*, *46*(14), 8000–8008. https://doi.org/10.1029/2019GL082493

Tsuchiya, T. (2011). Elasticity of subducted basaltic crust at the lower mantle pressures: Insights on the nature of deep mantle heterogeneity. *Physics of the Earth and Planetary Interiors*, *188*(3–4), 142–149. https://doi.org/10.1016/j.pepi.2011.06.018

Vanacore, E. A., Rost, S., & Thorne, M. S. (2016). Ultralow-velocity zone geometries resolved by multidimensional waveform modeling. *Geophysical Journal International*, *206*(1), 659–674. https://doi.org/10.1093/gji/ggw114

van der Hilst, R. D., de Hoop, M. V., Wang, P., Shim, S.-H., Ma, P., & Tenorio, L. (2007). Seismostratigraphy and thermal structure of Earth's core-mantle boundary region. *Science*, *315*(5820), 1813–1817. https://doi.org/10.1126/science.1137867

Vidale, J. E., & Hedlin, M. A. H. (1998). Evidence for partial melt at the core-mantle boundary north of Tonga from the strong scattering of seismic waves. *Nature*, *391*(6668), 682–685. https://doi.org/10.1038/35601

Walker, A. M., Forte, A. M., Wookey, J., Nowacki, A., & Kendall, J.-M. (2011). Elastic anisotropy of D" predicted from global models of mantle flow. *Geochemistry, Geophysics, Geosystems*, *12*(10). https://doi.org/10.1029/2011GC003732

Wang, W., Xu, Y., Sun, D., Ni, S., Wentzcovitch, R. M., & Wu, Z. (2020). Velocity and density characteristics of subducted oceanic crust and the origin of lower-mantle heterogeneities. *Nature Communications*, *11*(64), 64. https://doi.org/10.1038/s41467-019-13720-2

Ward, J., Nowacki, A., & Rost, S. (2020). Lateral velocity gradients in the African lower mantle inferred from slowness space observations of multipathing. *Geochemistry, Geophysics, Geosystems*, *21*(8), e2020GC009025. https://doi.org/10.1029/2020GC009025

Ward, J., Thorne, M. S., Nowacki, A., & Rost, S. (2021). Automatic slowness vector measurements of seismic arrivals with uncertainty estimates using bootstrap sampling, array methods and unsupervised learning. *Geophysical Journal International*, *226*(3), 1847–1857. https://doi.org/10.1093/gji/ggab196

Ward, J., Thorne, M. S., Nowacki, A., & Rost, S. (2023). Upper mantle structure beneath the contiguous US resolved with array observations of SKS multipathing and slowness vector perturbations. *Journal of Geophysical Research: Solid Earth*, *128*(7). https://doi.org/10.1029/2022JB026260

Waszek, L., Thomas, C., & Deuss, A. (2015). PKP precursors: Implications for global scatterers. *Geophysical Research Letters*, *42*(10), 3829–3838. https://doi.org/10.1002/2015GL063869

Wen, L. (2000). Intense seismic scattering near the Earth's core-mantle boundary beneath the Comores hotspot. *Geophysical Research Letters*, *27*(22), 3627–3630. https://doi.org/10.1029/2000gl011831

Whittaker, S., Thorne, M. S., Schmerr, N. C., & Miyagi, L. (2016). Seismic array constraints on the D" discontinuity beneath Central America. *Journal of Geophysical Research: Solid Earth*, *120*, 1–18. https://doi.org/10.1002/2015JB012392

Williams, Q., & Garnero, E. J. (1996). Seismic evidence for partial melt at the base of Earth's mantle. *Science*, *273*(5281), 1528–1530. https://doi.org/10.1126/science.273.5281.1528

Wolf, J., Long, M. D., & Frost, D. A. (2024). Ultralow velocity zone and deep mantle flow beneath the Himalayas linked to subducted slab. *Nature Geoscience*, *17*(4), 302–308. https://doi.org/10.1038/s41561-024-01386-5

Wright, C. (1975). The origin of short-period precursors to PKP. *Bulletin of the Seismological Society of America*, *65*(3), 765–786. https://doi.org/10.1785/bssa0650030765

Yao, J., & Wen, L. (2014). Seismic structure and ultra-low velocity zones at the base of the Earth's mantle beneath Southeast Asia. *Physics of the Earth and Planetary Interiors*, *233*, 103–111. https://doi.org/10.1016/j.pepi.2014.05.009

Yoshida, M. (2008). Core-mantle boundary topography estimated from numerical simulations of instantaneous mantle flow. *Geochemistry, Geophysics, Geosystems*, *9*(7). https://doi.org/10.1029/2008GC002008

Yu, S. (2020). *Extreme seismic anomalies near Earth's core mantle boundary* (PhD Dissertation thesis). (p. 208). Arizona State University.

Yu, S., & Garnero, E. J. (2018). Ultralow velocity zone locations: A global assessment. *Geochemistry, Geophysics, Geosystems*, *19*(2), 1–19. https://doi.org/10.1002/2017GC007281

References From the Supporting Information

Seton, M., Müller, R., Zahirovic, S., Gaina, C., Torsvik, T., Shephard, G., et al. (2012). Global continental and ocean basin reconstructions since 200Ma. *Earth-Science Reviews*, *113*(3–4), 212–270. https://doi.org/10.1016/j.earscirev.2012.03.002

Tackley, P. J., & King, S. D. (2003). Testing the tracer ratio method for modeling active compositional fields in mantle convection simulations. *Geochemistry, Geophysics, Geosystems*, *4*(4), 1–15. https://doi.org/10.1029/2001GC000214

Zhong, S. (2006). Constraints on thermochemical convection of the mantle from plume heat flux, plume excess temperature, and upper mantle temperature. *Journal of Geophysical Research*, *111*(B04409), 1–18. https://doi.org/10.1029/2005JB003972

Zhong, S., McNamara, A., Tan, E., Moresi, L., & Gurnis, M. (2008). A benchmark study on mantle convection in a 3-D spherical shell using CitcomS. *Geochemistry, Geophysics, Geosystems*, *9*(10). https://doi.org/10.1029/2008GC002048